

Improved theoretical analysis and design guidelines of a two-degree-of-freedom galloping piezoelectric energy harvester

Journal of Intelligent Material Systems and Structures

2022, Vol. 33(1) 210–230

© The Author(s) 2021

Article reuse guidelines:

sagepub.com/journals-permissions

DOI: 10.1177/1045389X211011681

journals.sagepub.com/home/jim



Guobiao Hu¹, Junrui Liang¹ , Lihua Tang²  and Junlei Wang³

Abstract

This paper presents an improved analysis of a two-degree-of-freedom (2DOF) galloping-based piezoelectric energy harvester (GPEH). First, an overview of the 2DOF GPEH, together with some discussions on its physical implementation, are presented. The theoretical model of the 2DOF GPEH is then developed. The analytical solutions are derived using the harmonic balance method. The dynamic behaviour of the 2DOF GPEH is predicted according to the solution characteristics. Moreover, the mode activation mechanism of the 2DOF GPEH is theoretically unveiled: depending on the system parameters; there may exist a single or multiple stable solutions which correspond to different vibration modes of the 2DOF GPEH. Subsequently, an equivalent circuit model of the 2DOF GPEH is established. Circuit simulations are performed to verify the analytical solutions. Case studies through detailed theoretical analysis and circuit simulation give in-depth insights into the dynamic behaviour of the 2DOF GPEH. It is demonstrated that by tuning the stiffness of the auxiliary oscillator, either the first or the second mode vibration of the 2DOF GPEH can be activated, resulting in completely different dynamic behaviours and energy harvesting performance. Finally, from the perspectives of reducing the cut-in wind speed and improving the voltage output, several design guidelines are provided.

Keywords

Galloping, energy harvesting, two-degree-of-freedom, mode activation

1. Introduction

The fast development and wide application of micro-electro-mechanical systems (MEMS), for example, wireless sensors, put forward an urgent demand to address the power supply issue for realising sustainable operation (Fang et al., 2019; Jo et al., 2020; Priya and Inman, 2009; Tang et al., 2013). Under certain circumstances where the devices are placed in remote regions, risk areas with high radiations or human bodies (i.e. medical implants), replacing or recharging conventional batteries becomes difficult. Energy harvesting technology has been proposed and developed in the past two decades to provide a viable solution by harnessing energy from surrounding sources, including solar power, vibration, heat, wind, to name a few.

Wind is one of the ubiquitous and predominant sources of renewable energy for large-scale power generation (Staggs et al., 2017). Employing wind for small-scale power generation to provide sustainable energy supply to MEMS has also attracted numerous research interests in recent years (Abdelkefi, 2016; Wang et al., 2020a). Different from a windmill, the size of a wind

energy harvester is often required to be compact to meet the miniaturisation requirement of MEMS. Hence, instead of rotary turbine design, small scale wind energy harvesters are often designed based on flow-induced vibration mechanisms and phenomena, including galloping (Ali et al., 2013; Barrero-Gil et al., 2010; Sirohi and Mahadik, 2012), vortex-induced vibration (VIV) (Wang et al., 2019a; Zhang et al., 2020), wake galloping (Liu et al., 2020; Yan et al.,

¹School of Information Science and Technology, ShanghaiTech University, Shanghai, China

²Department of Mechanical Engineering, University of Auckland, Auckland, New Zealand

³School of Mechanical and Power Engineering, Zhengzhou University, Zhengzhou, China

Corresponding authors:

Lihua Tang, Department of Mechanical Engineering, University of Auckland, 20 Symonds Street, Auckland 1010, New Zealand.

Email: l.tang@auckland.ac.nz

Junlei Wang, School of Mechanical and Power Engineering, Zhengzhou University, 100 Science Road, Zhengzhou 450001, China.

Email: jlwang@zzu.edu.cn

2020) and flutter (Eugeni et al., 2020). Since galloping can lead to the self-excited vibration around the natural frequency of the system, the consequent limit cycle motion near resonance has a large oscillation amplitude. Moreover, as compared to VIV, the galloping phenomenon can occur over a much wider range of wind speed. For the above two reasons, galloping-based energy harvesters have been extensively studied in the past few years.

The cut-in wind speed and the power/voltage output amplitude are the two main concerns of a galloping energy harvester. The cut-in wind speed is the critical wind speed when the galloping energy harvester starts to vibrate and generate power. From the energy harvesting perspective, it is evident that lower cut-in wind speed and higher power output are preferred. The dynamic behaviour of a galloping energy harvester strongly depends on the aerodynamic force characteristic determined by the cross-section geometry of the bluff body. Common bluff bodies include triangle-sectioned (Sirohi and Mahadik, 2011; Wang et al., 2019b), square-sectioned (Abdelkefi et al., 2012; Hu et al., 2019, 2021a) and D-shape sectioned shapes (Sirohi and Mahadik, 2012; Zhao and Yang, 2018). Research have been conducted to compare the bluff bodies (Yang et al., 2013) and optimize them (Wang et al., 2019c) to improve the energy harvesting performance of GPEHs. Besides the bluff body, from the mechanical structure point of view, researchers also explored various innovative configurations to improve the performance of GPEHs. Following the track of the development of vibration energy harvesters (VEHs), researchers introduced nonlinearities into mechanical structures to improve the galloping energy harvesting performance. For example, Bibo et al. (2015) proposed and studied a bistable GPEH that contained four magnets to form a nonlinear restoring force. It was found in their experiment that once the inter-well motion of the bistable GPEH was activated, the power output could become much larger than a conventional linear GPEH. More related works of employing various nonlinearities in wind energy harvesting can be found in (Alhadidi et al., 2016; Ewera et al., 2014; Naseer et al., 2017; Yang et al., 2019).

According to the authors' best knowledge, different from vibration energy harvesting, lots of previous galloping energy harvesters were designed and modelled as SDOF systems. To avoid misunderstanding and controversies, we would like to remind the readers that unlike galloping energy harvesters, other flow-induced vibration based energy harvesters, such as the flutter-based energy harvester reported in (Bryant and Garcia, 2011), are often considered to have at least two degrees of freedom. In relatively more recent, still similar to the track of the development of vibration energy harvesters: evolving from SDOF VEH (Erturk and Inman, 2008) to 2DOF (even multiple-degree-of-freedom (MDOF))

VEH (Tang and Yang, 2012), Lan et al. (2019) proposed to extend the SDOF system to 2DOF system for galloping energy harvesting. This pioneering work presented an analytical analysis of two configurations of 2DOF GPEH modelled with lumped parameters. A parametric study was performed to investigate the effects of various system parameters on the performance of the 2DOF GPEH. Hu et al. (2021a) prototyped a 2DOF GPEH using practical beam structures and conducted an experimental study. Some phenomena (e.g. the activation of the second vibration mode) different from the analytical predictions in (Lan et al., 2019) were experimentally observed. Though a simple theoretical model was used to successfully explain the interesting phenomena in (Hu et al., 2021a), there lacks an in-depth understanding of the mechanisms behind those behaviours and phenomena.

In fact, the modal activation problem for multiple-degree-of-freedom galloping systems has been noticed and investigated by researchers before. Blevins and Iwan (1974) investigated the galloping response of a two-degree-of-freedom system that had a translational-DOF and a rotational-DOF. The asymmetric technique was used to derive the approximate steady-state solution. Under a constant wind speed, the mode behaviour was found to vary with the change of the system parameters. When the system parameters were tuned coincidentally to meet a certain condition, even internal resonance could take place, and an energy transfer effect could occur. Desai et al. (1990) performed a further study of the same 2DOF galloping system as presented in (Blevins and Iwan, 1974) by utilising the averaging method. A more recent relevant research on a similar topic can be found in (Yu, 2016). However, these studies considered the galloping responses of 2DOF systems with both translational and torsional displacements, originating from the galloping phenomenon associated with an iced transmission line. Luongo and Di Fabio (1993) studied the multimodal galloping phenomenon in a periodic slender structure that had multiple natural frequencies in one or more bands. However, that model is still quite different from the one of our interest. From the literature review, the mode activation problem has attracted few attention from the researchers in the field of galloping energy harvesting, though it might bring a significant influence on the dynamic systems. For limited existing studies of 2DOF GPEHs, the analyses reported in the literature are relatively deficient, and the mode activation problem has not been discussed yet due to the lack of a solid theoretical foundation.

In this paper, based on the work by Hu et al. (2021a) and Lan et al. (2019), an improved analysis of a 2DOF GPEH is presented. The analytical solution derived by Lan et al. (2019) only contains the fundamental frequency component. It is valid for some limited cases, which is the reason why the analytical model in (Lan

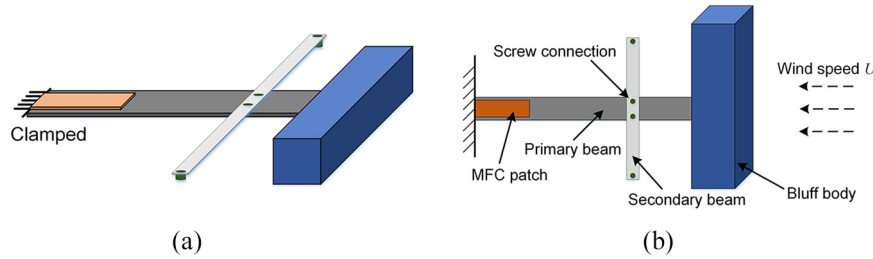


Figure 1. (a) Three-dimensional model of the 2DOF GPEH and (b) the top view with annotations of different components. (Hu et al., 2021a).

et al., 2019) can not be used to explain the experimental phenomena in (Hu et al., 2021a). The rest of the paper is organized as follows. In section 2, the 2DOF GPEH system is reviewed. The equivalence between the physical model in (Hu et al., 2021a) and a 2DOF dynamic system is briefly explained. In section 3, the theoretical model of the 2DOF GPEH is developed, and the analytical solution is derived. In section 4, the solution characteristics are discussed and analysed to explain the mode activation mechanism of the 2DOF GPEH. In section 5, an equivalent circuit model of the 2DOF GPEH is established to verify the analytical solutions. In section 6, specific case studies are considered to give in-depth insights into the dynamic characteristics of the 2DOF GPEH. Moreover, the analytical results are validated by equivalent circuit simulation results. In section 7, several design guidelines are proposed to help the development of the kind of 2DOF GPEH with desirable energy harvesting performance. Conclusions are summarized in section 8.

2. Overview of 2DOF GPEH system

Figure 1 shows the schematic of the 2DOF GPEH proposed in (Hu et al., 2021a). Although an experimental study has been conducted and interesting phenomena have been observed and reported in (Hu et al., 2021a), there lacks a solid theoretical model to provide an in-depth explanation of the dynamic behaviour of the 2DOF GPEH. For conciseness but without loss of completeness, the construction of the 2DOF GPEH is

briefly introduced as follows. More details including the physical prototyping can be referred to (Hu et al., 2021a).

The 2DOF GPEH mainly consists of a primary beam and a secondary beam, playing the roles as the primary and auxiliary oscillators. A piezoelectric transducer is bonded at the root of the primary beam to realize energy transduction. A bluff body is attached at the tip of the primary beam, serving as the tip mass and the object where the aerodynamic force applies. The reason that the secondary beam is symmetrically designed has been explained in (Hu et al., 2021a). Screws are used for beam connection and also as tip mass of the secondary beam to tune its natural frequency.

Before proceeding to the theoretical modelling of the 2DOF GPEH, the equivalence between the system presented in Figure 1 and a 2DOF system is quickly explained. More detailed and rigorous mathematical derivations can be referred to (Hu et al., 2020, 2021b). To represent the continuous system presented in Figure 1 with lumped parameters, the primary beam and the secondary beam are separately represented as two independent SDOF systems. For the primary beam, we approximate its fundamental mode shape by the static deflection. The equivalent lumped parameters can then be derived. The detailed derivation procedure can be referred to (Hu et al., 2018, 2019). The explicit expressions of the equivalent lumped parameters including the equivalent stiffness k_2 , mass m_2 , damping coefficient c_2 and the electromechanical coupling coefficient θ are listed below for reminding readers about the key results in those papers.

$$\begin{cases} k_2 = \frac{3EI_p EI_s}{EI_p L_s^3 + 3EI_s L_p L_s^2 + 3EI_p L_p^2 L_s + EI_s L_p^3} \\ m_2 = \frac{k_2}{\omega_n^2} + M_{t2} \\ c_2 = 2\zeta_2 \sqrt{k_2 m_2} \\ \theta = \vartheta \frac{4EI_s L_p^3 m_p + 12EI_s L_p L_s (L_p + L_s) m_s + 12EI_s L_p (L_p + 2L_s) M_{t2}}{\left\{ EI_s L_p^3 (3L_p + 4L_s) m_p + [3EI_p L_s^4 + EI_s L_p L_s (12L_s^2 + 18L_p L_s + 8L_p^2)] m_s \right\} + 8 [EI_p (L_p^3 + L_s^3) + 3EI_s L_p L_s (L_p + L_s)] M_{t2}} \end{cases} \quad (1)$$

where m_p and m_s are the masses per unit length. EI_p and EI_s are the bending stiffnesses. The subscripts p and s denote the beam sections with and without piezoelectric coverage, respectively. Their lengths are, respectively, of L_p and L_s . M_{t2} is the mass of the bluff body. $\vartheta = -e_{31}b_p h_{pc}$ is the piezoelectric coupling term. ω_n is the natural frequency of the system consisting of the primary beam and the piezoelectric transducer, but without the bluff body. ζ_2 is the damping ratio of the fundamental mode of the piezoelectric covered primary beam with the bluff body. Similarly, the secondary beam can also be represented as an SDOF system following the above procedure. The equivalent lumped parameters of the secondary beam can be obtained as

$$\begin{cases} m_1 = 2 \times \left(\frac{13}{54} m_r L_r + M_{t1} \right) \\ k_1 = 2 \times \frac{3EI_r}{L_r^3} \\ c_1 = 2 \times 2\zeta_1 \sqrt{m_1 k_1} \end{cases} \quad (2)$$

where m_r is the mass per unit length and EI_r is the bending stiffness of the secondary beam. L_r is the half of the length of the secondary beam and M_{t1} is the tip mass (i.e. weight of the screw). ζ_1 is the damping ratio of the fundamental mode of the secondary beam. It is worth noting that since the secondary beam is split into two identical cantilever beams by the primary beam, when converting the secondary beam into an equivalent SDOF oscillator, the equivalent lumped parameters (i.e. m_1 , k_1 and c_1) of the secondary beam should double those of a single cantilever.

It should be mentioned that the SDOF representation is only valid under the assumption that all the lumped parameters are concentrated at the tip of the cantilever beam. In other words, the derived lumped parameters (i.e. equation (2)) are only effective at the beam tip. While, the coupling between the secondary beam and the primary beam is through the force interaction at the root of the secondary beam. By considering the relationship between the actual reaction force of the secondary beam using the beam theory and the reaction force calculated using the SDOF model, a reaction force correction factor should be introduced to address this issue. Moreover, the mounting position of the secondary beam also has an important influence, for which a scaling factor should be introduced to take such an effect into account. The details of a series of factors to guarantee the successful establishment of the 2DOF model can be referred to (Hu et al., 2020, 2021b). The accuracy of the equivalent 2DOF model has already been quantitatively verified in (Hu et al., 2020, 2021b) by comparing it with the original continuous model presented in Figure 1. Therefore, the model

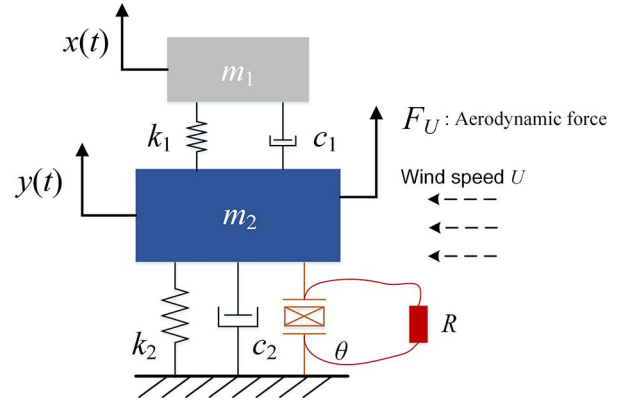


Figure 2. Schematic of the 2DOF GPEH under investigation in this study.

presented in Figure 1 can be reasonably treated as a 2DOF GPEH.

3. Theoretical modelling

Though an accurate 2DOF model can be obtained to describe the system presented in Figure 1 by following the procedures in (Hu et al., 2020, 2021b), various factors in the governing equations make the mathematical formulas become relatively complicated. Therefore, without loss of generality but only for simplicity, those correction factors are not considered, and the governing equations of an ordinary 2DOF GPEH model will be employed for the following theoretical modelling.

3.1. Governing equations

The governing equations of the 2DOF GPEH shown in Figure 2 can be written as:

$$m_1 \ddot{x}(t) + c_1(\dot{x}(t) - \dot{y}(t)) + k_1(x(t) - y(t)) = 0 \quad (3)$$

$$\begin{aligned} m_2 \ddot{y}(t) + c_2 \dot{y}(t) + k_2 y(t) + c_1(\dot{y}(t) - \dot{x}(t)) \\ + k_1(y(t) - x(t)) + \theta v(t) \\ = \frac{1}{2} \rho U^2 L D_B \left(s_1 \left(\frac{\dot{y}(t)}{U} \right) - s_3 \left(\frac{\dot{y}(t)}{U} \right)^3 \right) \end{aligned} \quad (4)$$

$$C_p \dot{v}(t) + \frac{v(t)}{R} = \theta \dot{y}(t) \quad (5)$$

where m_i , k_i and c_i are the mass, stiffness and damping coefficient, respectively. The subscript $i = 1$ and 2 denote the auxiliary and the primary oscillators, respectively. $x(t)$ and $y(t)$ represent the displacements of the auxiliary and the primary oscillators, respectively. ρ is the air density. U is the wind speed. L and D_B are the cross-flow length and width of the bluff body. s_1 and s_3 are the empirical linear and cubic coefficients of the

transverse galloping force, which are dependent on the cross-section geometry of the prismatic structure. θ and C_p are the electromechanical coupling coefficient and the clamped capacitance of the piezoelectric transducer. $v(t)$ is the voltage across the load resistance R .

3.2. Approximate analytical solution

Since the 2DOF GPEH has two natural frequencies, the displacement response of the auxiliary oscillator is assumed to be in the form of the superposition of two harmonic functions.

$$x(t) = x_a(t) + x_b(t) \quad (6)$$

where $x_a(t)$ and $x_b(t)$, respectively, correspond to the harmonic responses of the first and the second natural frequencies of the 2DOF GPEH. To be more specific,

$$x_a(t) = a_1(t) \sin(\omega_1 t) + b_1(t) \cos(\omega_1 t) \quad (7)$$

$$x_b(t) = g_1(t) \sin(\omega_2 t) + h_1(t) \cos(\omega_2 t) \quad (8)$$

Similarly, the displacement response of the primary oscillator is also assumed in the form as:

$$y(t) = y_a(t) + y_b(t) \quad (9)$$

$$y_a(t) = a_2(t) \sin(\omega_1 t) + b_2(t) \cos(\omega_1 t) \quad (10)$$

$$y_b(t) = g_2(t) \sin(\omega_2 t) + h_2(t) \cos(\omega_2 t) \quad (11)$$

The amplitudes of the first and second harmonic components with the frequencies of ω_1 and ω_2 are defined as:

$$\begin{cases} (r_1(t))^2 = (a_2(t))^2 + (b_2(t))^2 \\ (r_2(t))^2 = (g_2(t))^2 + (h_2(t))^2 \end{cases} \quad (12)$$

As the piezoelectric transducer is directly coupled with the primary oscillator, the voltage response can be presumed in a similar form as well.

$$v(t) = v_a(t) + v_b(t) \quad (13)$$

$$v_a(t) = v_1(t) \sin(\omega_1 t) + v_2(t) \cos(\omega_1 t) \quad (14)$$

$$v_b(t) = v_3(t) \sin(\omega_2 t) + v_4(t) \cos(\omega_2 t) \quad (15)$$

Substituting equations (9) and (13) into equation (5), omitting the higher harmonics and balancing the terms of $\sin(\omega_1 t)$, $\cos(\omega_1 t)$, $\sin(\omega_2 t)$ and $\cos(\omega_2 t)$, one obtains:

$$\begin{cases} -C_p v_2(t) \omega_1 + \frac{v_1(t)}{R} + \theta b_2(t) \omega_1 = 0 \\ C_p v_1(t) \omega_1 + \frac{v_2(t)}{R} - \theta a_2(t) \omega_1 = 0 \\ -C_p v_4(t) \omega_2 + \frac{v_3(t)}{R} + \theta h_2(t) \omega_2 = 0 \\ C_p v_3(t) \omega_2 + \frac{v_4(t)}{R} - \theta g_2(t) \omega_2 = 0 \end{cases} \quad (16)$$

Note that the derivatives are forced to be zeros for the steady-state condition. Solving equation (16), we can represent $v_1(t) \sim v_4(t)$ by $a_2(t) \sim h_2(t)$:

$$\begin{cases} v_1(t) = \frac{K_{e1} a_2(t)}{\theta} - \frac{C_{e1} b_2(t)}{\theta} \\ v_2(t) = \frac{C_{e1} a_2(t)}{\theta} + \frac{K_{e1} b_2(t)}{\theta} \\ v_3(t) = \frac{K_{e2} g_2(t)}{\theta} - \frac{C_{e2} h_2(t)}{\theta} \\ v_4(t) = \frac{C_{e2} g_2(t)}{\theta} + \frac{K_{e2} h_2(t)}{\theta} \end{cases} \quad (17)$$

where $K_{e1} = \frac{R^2 \theta^2 \omega_1^2 C_p}{C_p^2 R^2 \omega_1^2 + 1}$, $C_{e1} = \frac{\theta^2 \omega_1 R}{C_p^2 R^2 \omega_1^2 + 1}$, $K_{e2} = \frac{R^2 \theta^2 \omega_2^2 C_p}{C_p^2 R^2 \omega_2^2 + 1}$ and $C_{e2} = \frac{\theta^2 \omega_2 R}{C_p^2 R^2 \omega_2^2 + 1}$. Thus, the voltage response can be expressed using $y_a(t)$ and $y_b(t)$:

$$v(t) = \frac{K_{e1} y_a(t)}{\theta} + \frac{K_{e2} y_b(t)}{\theta} + \frac{C_{e1} \dot{y}_a(t)}{\theta \omega_1} + \frac{C_{e2} \dot{y}_b(t)}{\theta \omega_2} \quad (18)$$

Substituting equation (18) into the governing equations can completely eliminate the unknown variable $v(t)$. And one can now focus on the governing equations constituted of equations (3) and (4) only. The mathematical formulation of the whole problem is thus greatly simplified. Substituting equations (6) and (9) into equations (3) and (4), balancing the coefficients of the terms $\sin(\omega_1 t)$ and $\cos(\omega_1 t)$ and forcing the derivatives to be zero for the steady-state condition, one obtains:

$$(-m_1 \omega_1^2 + k_1) a_1(t) + b_2(t) c_1 \omega_1 - b_1(t) c_1 \omega_1 - a_2(t) k_1 = 0 \quad (19)$$

$$\begin{aligned} a_1(t) c_1 \omega_1 - a_2(t) c_1 \omega_1 + (-m_1 \omega_1^2 + k_1) b_1(t) \\ - b_2(t) k_1 = 0 \end{aligned} \quad (20)$$

$$\begin{aligned} -a_1(t) k_1 + (-m_2 \omega_1^2 + K_{e1} + k_1 + k_2) a_2(t) \\ + b_1(t) c_1 \omega_1 + (-c_1 \omega_1 - c_2 \omega_1 - C_{e1}) b_2(t) \\ = \frac{b_2(t)}{8U} (3D_B L (r_1(t))^2 \rho s_3 \omega_1^3 + 6D_B L (r_2(t))^2 \rho s_3 \omega_1 \omega_2^2 \\ - 4U^2 \rho L D_B s_1 \omega_1) \end{aligned} \quad (21)$$

$$\begin{aligned} -a_1(t) c_1 \omega_1 + (c_1 \omega_1 + c_2 \omega_1 + C_{e1}) a_2(t) - b_1(t) k_1 \\ + (-m_2 \omega_1^2 + K_{e1} + k_1 + k_2) b_2(t) \\ = \frac{a_2(t)}{8U} (-3D_B L (r_1(t))^2 \rho s_3 \omega_1^3 - 6D_B L (r_2(t))^2 \rho \\ s_3 \omega_1 \omega_2^2 + 4U^2 \rho L D_B s_1 \omega_1) \end{aligned} \quad (22)$$

Solving equations (19) and (20) simultaneously gives:

$$\begin{cases} a_1(t) = P_1 a_2(t) + Q_1 b_2(t) \\ b_1(t) = -Q_1 a_2(t) + P_1 b_2(t) \end{cases} \quad (23)$$

$$\text{where } \begin{cases} P_1 = \frac{c_1^2 \omega_1^2 - k_1 m_1 \omega_1^2 + k_1^2}{m_1^2 \omega_1^4 + c_1^2 \omega_1^2 - 2k_1 m_1 \omega_1^2 + k_1^2} \\ Q_1 = \frac{c_1 m_1 \omega_1^3}{m_1^2 \omega_1^4 + c_1^2 \omega_1^2 - 2k_1 m_1 \omega_1^2 + k_1^2} \\ P_2 = -\frac{c_1 m_1 \omega_1^3}{m_1^2 \omega_1^4 + c_1^2 \omega_1^2 - 2k_1 m_1 \omega_1^2 + k_1^2} \\ Q_2 = -\frac{-c_1^2 \omega_1^2 + k_1 m_1 \omega_1^2 - k_1^2}{m_1^2 \omega_1^4 + c_1^2 \omega_1^2 - 2k_1 m_1 \omega_1^2 + k_1^2} \end{cases}.$$

Substituting equation (23) into equations (21) and (22) eliminates $a_1(t)$ and $b_1(t)$, and degenerates the set of equations as:

$$\begin{aligned} & (-Q_1 c_1 \omega_1 - m_2 \omega_1^2 - P_1 k_1 + K_{e1} + k_1 + k_2) a_2(t) \\ & + (P_1 c_1 \omega_1 - Q_1 k_1 - c_1 \omega_1 - c_2 \omega_1 - C_{e1}) b_2(t) \\ & = \frac{b_2(t)}{8U} (3D_B L(r_1(t))^2 \rho s_3 \omega_1^3 + 2D_B L(r_2(t))^2 \rho s_3 \omega_1 \omega_2^2 \\ & - 4U^2 \rho L D_B s_1 \omega_1) \end{aligned} \tag{24}$$

$$\begin{aligned} & (-P_1 c_1 \omega_1 + Q_1 k_1 + c_1 \omega_1 + c_2 \omega_1 + C_{e1}) a_2(t) \\ & + (-Q_1 c_1 \omega_1 - m_2 \omega_1^2 - P_1 k_1 + K_{e1} + k_1 + k_2) b_2(t) \\ & = \frac{a_2(t)}{8U} (-3D_B L(r_1(t))^2 \rho s_3 \omega_1^3 - 2D_B L(r_2(t))^2 \rho s_3 \omega_1 \omega_2^2 \\ & + 4U^2 \rho L D_B s_1 \omega_1) \end{aligned} \tag{25}$$

Summing equation (24) $\times b_2(t)$ and equation (25) $\times a_2(t)$, then after some mathematical treatment, we have:

$$\begin{aligned} & (-m_1 \omega_1^2 + k_1)(m_1 m_2 \omega_1^4 - K_{e1} m_1 \omega_1^2 - k_1 m_1 \omega_1^2 \\ & - k_1 m_2 \omega_1^2 - k_2 m_1 \omega_1^2 + K_{e1} k_1 + k_1 k_2) = 0 \end{aligned} \tag{26}$$

which is the implicit expression that implies the solution to the frequency of the self-oscillation that is, ω_1 . On the other hand, subtracting equation (24) $\times b_2(t)$ by equation (25) $\times a_2(t)$ gives:

$$\begin{aligned} & (r_1(t))^2 P_1 c_1 \omega_1 - (r_1(t))^2 Q_1 k_1 - (r_1(t))^2 c_1 \omega_1 - (r_1(t))^2 \\ & c_2 \omega_1 - C_{e1} (r_1(t))^2 \\ & = \frac{1}{8U} (3D_B L(r_1(t))^4 \rho s_3 \omega_1^3 + 6D_B L(r_1(t))^2 \\ & (r_2(t))^2 \rho s_3 \omega_1 \omega_2^2 - 4D_B L(r_1(t))^2 U^2 \rho s_1 \omega_1) \end{aligned} \tag{27}$$

which is the implicit expression that contains the relationship between $r_1(t)$ and $r_2(t)$. To solve the two unknown variables, one more equation that contains the relationship between $r_1(t)$ and $r_2(t)$ is to be sought. Applying the similar process to equations (3) and (4) by substituting into equations (6) and (9), balancing the coefficients of the terms $\sin(\omega_2 t)$ and $\cos(\omega_2 t)$, and

forcing the derivatives to be zero for the steady-state condition, one obtains:

$$(-m_1 \omega_2^2 + k_1) g_1(t) - c_1 h_1(t) \omega_2 + h_2(t) c_1 \omega_2 - g_2(t) k_1 = 0 \tag{28}$$

$$-h_1(t) m_1 \omega_2^2 + g_1(t) c_1 \omega_2 - g_2(t) c_1 \omega_2 + h_1(t) k_1 - h_2(t) k_1 = 0 \tag{29}$$

$$\begin{aligned} & (-m_2 \omega_2^2 + K_{e2} + k_1 + k_2) g_2(t) + (-c_1 \omega_2 - c_2 \omega_2 - C_{e2}) \\ & h_2(t) + c_1 h_1(t) \omega_2 - g_1(t) k_1 \\ & = \frac{h_2(t)}{8U} (6D_B L(r_1(t))^2 \rho s_3 \omega_1^2 \omega_2 + 3D_B L(r_2(t))^2 \rho s_3 \omega_2^3 \\ & - 4D_B L U^2 \rho s_1 \omega_2) \end{aligned} \tag{30}$$

$$\begin{aligned} & (c_1 \omega_2 + c_2 \omega_2 + C_{e2}) g_2(t) + (-m_2 \omega_2^2 + K_{e2} + k_1 + k_2) \\ & h_2(t) - g_1(t) c_1 \omega_2 - h_1(t) k_1 \\ & = \frac{g_2(t)}{8U} (-6D_B L(r_1(t))^2 \rho s_3 \omega_1^2 \omega_2 - 3D_B L(r_2(t))^2 \rho s_3 \omega_2^3 \\ & + 4D_B L U^2 \rho s_1 \omega_2) \end{aligned} \tag{31}$$

Based on equations (28) and (29), we can represent $g_1(t)$ and $h_1(t)$ by $g_2(t)$ and $h_2(t)$:

$$\begin{cases} g_1(t) = K_1 h_2(t) + J_1 g_2(t) \\ h_1(t) = J_1 h_2(t) - K_1 g_2(t) \end{cases} \tag{32}$$

$$\text{where } \begin{cases} J_1 = \frac{c_1^2 \omega_2^2 - k_1 m_1 \omega_2^2 + k_1^2}{m_1^2 \omega_2^4 + c_1^2 \omega_2^2 - 2k_1 m_1 \omega_2^2 + k_1^2} \\ K_1 = \frac{c_1^2 \omega_2^2 - k_1 m_1 \omega_2^2 + k_1^2}{m_1^2 \omega_2^4 + c_1^2 \omega_2^2 - 2k_1 m_1 \omega_2^2 + k_1^2} \\ J_2 = -\frac{c_1 m_1 \omega_2^3}{m_1^2 \omega_2^4 + c_1^2 \omega_2^2 - 2k_1 m_1 \omega_2^2 + k_1^2} \\ K_2 = \frac{c_1^2 \omega_2^2 - k_1 m_1 \omega_2^2 + k_1^2}{m_1^2 \omega_2^4 + c_1^2 \omega_2^2 - 2k_1 m_1 \omega_2^2 + k_1^2} \end{cases}.$$

By substituting equation (32) into equations (30) and (31), $g_1(t)$ and $h_1(t)$ are eliminated. The set of equations are simplified and become:

$$\begin{aligned} & (-K_1 c_1 \omega_2 - m_2 \omega_2^2 - J_1 k_1 + K_{e2} + k_1 + k_2) g_2(t) \\ & + (J_1 c_1 \omega_2 - K_1 k_1 - c_1 \omega_2 - c_2 \omega_2 - C_{e2}) h_2(t) \\ & = \frac{h_2(t)}{8U} (3D_B L(r_2(t))^2 \rho s_3 \omega_2^3 + 6D_B L(r_1(t))^2 \rho s_3 \omega_1^2 \omega_2 \\ & - 4U^2 \rho L D_B s_1 \omega_2) \end{aligned} \tag{33}$$

$$\begin{aligned} & (-J_1 c_1 \omega_2 + K_1 k_1 + c_1 \omega_2 + c_2 \omega_2 + C_{e2}) g_2(t) \\ & + (-K_1 c_1 \omega_2 - m_2 \omega_2^2 - J_1 k_1 + K_{e2} + k_1 + k_2) h_2(t) \\ & = \frac{g_2(t)}{8U} (-6D_B L(r_1(t))^2 \rho s_3 \omega_1^2 \omega_2 - 3D_B L(r_2(t))^2 \rho s_3 \omega_2^3 \\ & + 4U^2 \rho L D_B s_1 \omega_2) \end{aligned} \tag{34}$$

After some mathematical treatment of the sum of equation (33) $\times h_2(t)$ and equation (34) $\times g_2(t)$, one obtains:

$$\begin{aligned} &(-m_1\omega_2^2 + k_1)(m_1m_2\omega_2^4 - K_{e2}m_1\omega_2^2 - k_1m_1\omega_2^2 \\ &-k_1m_2\omega_2^2 - k_2m_1\omega_2^2 + K_{e2}k_1 + k_1k_2) = 0 \end{aligned} \quad (35)$$

which is the implicit expression that implies the solution to ω_2 . Subtracting equation (33) $\times h_2(t)$ by equation (34) $\times g_2(t)$ yields:

$$\begin{aligned} &J_1(r_2(t))^2c_1\omega_2 - K_1(r_2(t))^2k_1 - (r_2(t))^2c_1\omega_2 - (r_2(t))^2 \\ &c_2\omega_2 - C_{e2}(r_2(t))^2 \\ &= \frac{1}{8U} (6D_B L(r_1(t))^2(r_2(t))^2\rho s_3\omega_1^2\omega_2 + 3D_B L(r_2(t))^4\rho \\ &s_3\omega_2^3 - 4D_B L(r_2(t))^2U^2\rho s_1\omega_2) \end{aligned} \quad (36)$$

which is the other equation that contains the relationship between $r_1(t)$ and $r_2(t)$ to be sought. Solving the two equations (27) and (36) simultaneously, the unknown variables $r_1(t)$ and $r_2(t)$ can be derived. It is noted that there exist three sets of non-trivial solutions as follows:

$$\begin{cases} r_1^2(t) = \frac{4U[D_B L U \rho s_1 \omega_1 + 2P_1 c_1 \omega_1 - 2Q_1 k_1 - 2(c_1 + c_2)\omega_1 - 2C_{e1}]}{3D_B L \rho s_3 \omega_1^3} \\ r_2^2(t) = 0 \end{cases} \quad (37)$$

$$\begin{cases} r_1^2(t) = 0 \\ r_2^2(t) = \frac{4U[D_B L U \rho s_1 \omega_2 + 2J_1 c_1 \omega_2 - 2K_1 k_1 - 2(c_1 + c_2)\omega_2 - 2C_{e2}]}{3D_B L \rho s_3 \omega_2^3} \end{cases} \quad (38)$$

$$\begin{cases} r_1^2(t) = \frac{4U \left[\frac{D_B L U \rho s_1 \omega_1 \omega_2 + 4J_1 c_1 \omega_1 \omega_2 - 2P_1 c_1 \omega_1 \omega_2 - 4K_1 k_1 \omega_1}{+ 2Q_1 k_1 \omega_2 - 2(c_1 + c_2)\omega_1 \omega_2 + 2C_{e1} \omega_2 - 4C_{e2} \omega_1} \right]}{9D_B L \rho s_3 \omega_1^3 \omega_2} \\ r_2^2(t) = \frac{4U \left[\frac{D_B L U \rho s_1 \omega_1 \omega_2 + 4P_1 c_1 \omega_1 \omega_2 - 2J_1 c_1 \omega_1 \omega_2 - 4Q_1 k_1 \omega_2}{+ 2K_1 k_1 \omega_1 - 2(c_1 + c_2)\omega_1 \omega_2 + 2C_{e2} \omega_1 - 4C_{e1} \omega_2} \right]}{9D_B L \rho s_3 \omega_1 \omega_2^3} \end{cases} \quad (39)$$

Whether the three sets of solutions exist depends on the signs of the computed values. Since the physical meanings of $r_1(t)$ and $r_2(t)$ are the displacement amplitudes of the limit cycles with the frequencies of ω_1 and ω_2 , respectively, one knows that a specific solution does exist only if $r_1^2(t) \geq 0$ and $r_2^2(t) \geq 0$. Temporarily putting aside of the existence issue of the solutions, from only the formulations of the solutions, we can find that the first and the second sets of solutions indicate single-frequency limit cycle oscillations (LCOs) with the frequencies of ω_1 and ω_2 , respectively. The third set of solution indicates a dual-frequency LCO motion. In retrospect to the aforementioned relationships between other unknown parameters and $r_1(t)$ and $r_2(t)$, all the

unknown variables can be consequently calculated. The voltage amplitudes of the harmonic components $v_a(t)$ and $v_b(t)$ with the frequencies of ω_1 and ω_2 are, respectively:

$$\begin{cases} V_a(t) = r_1(t) \sqrt{\left(\frac{K_{e1}}{\theta}\right)^2 + \left(\frac{C_{e1}}{\theta}\right)^2} \\ V_b(t) = r_2(t) \sqrt{\left(\frac{K_{e2}}{\theta}\right)^2 + \left(\frac{C_{e2}}{\theta}\right)^2} \end{cases} \quad (40)$$

3.3. Stability analysis

Due to the nonlinearity of the galloping induced force, it is found that there may exist multiple solutions (i.e. equations (37)–(39)). However, even if all the solutions mathematically exist, whether they are physically attainable depends on their stability characteristics. In this paper, the averaging method is employed to evaluate the stabilities of the solutions, since it can conveniently cast the governing equations of a complicated nonlinear system into a state-space form (Rudowski, 1982). For a classic SDOF GPEH, Javed et al. (2016) analysed the stabilities of the steady-state solutions based on the shooting method. Interested readers are recommended to also refer to that article, as the underlying principles are actually similar: stability analyses are based on evaluating the eigenvalues of relevant characteristic matrices. Considering the undamped free vibration of the 2DOF GPEH and neglecting the electromechanical coupling, one can derive the natural frequencies:

$$\omega_{1,2}^2 = \frac{1}{2m_1 m_2} [(k_1 + k_2)m_1 + k_1 m_2 \mp \sqrt{(m_1 + m_2)^2 k_1^2 + 2k_2 m_1 (m_1 - m_2) k_1 + k_2^2 m_1^2}] \quad (41)$$

The corresponding modes of the 2DOF system are:

$$\begin{pmatrix} 1 \\ p_i \end{pmatrix} = \begin{pmatrix} 1 \\ \frac{-m_1 \omega_i^2 + k_1}{k_1} \end{pmatrix} \quad (i = 1, 2) \quad (42)$$

After introducing the modal coordinates $u_1(t)$ and $u_2(t)$, the displacements of the auxiliary and primary oscillators can be expressed in the form as:

$$\begin{pmatrix} x(t) \\ y(t) \end{pmatrix} = \begin{bmatrix} 1 & 1 \\ p_1 & p_2 \end{bmatrix} \begin{pmatrix} u_1(t) \\ u_2(t) \end{pmatrix} \quad (43)$$

Similarly, the voltage across the load resistance can be written as:

$$\begin{aligned} v(t) &= \frac{C_{e1} p_1 \dot{u}_1(t)}{\theta \omega_1} + \frac{C_{e2} p_2 \dot{u}_2(t)}{\theta \omega_2} \\ &+ \frac{K_{e1} p_1 u_1(t) + K_{e2} p_2 u_2(t)}{\theta} \end{aligned} \quad (44)$$

Substituting equations (43) and (44) into equations (3) and (4), one obtains:

$$\begin{aligned}
\ddot{u}_1(t) + \omega_1^2 u_1(t) &= -\zeta_{11} \dot{u}_1(t) - \zeta_{12} \dot{u}_2(t) \\
&- \frac{p_1 \rho U L D_B}{2M_1} \left(s_1 (p_1 \dot{u}_1(t) + p_2 \dot{u}_2(t)) - \frac{s_3 (p_1 \dot{u}_1(t) + p_2 \dot{u}_2(t))^3}{U^2} \right) \\
&- \frac{p_1}{M_1} \left[\frac{C_{e1} p_1 \dot{u}_1(t)}{\omega_1} + \frac{C_{e2} p_2 \dot{u}_2(t)}{\omega_2} + K_{e1} p_1 u_1(t) + K_{e2} p_2 u_2(t) \right] \\
&= f_1(u_1(t), u_2(t), \dot{u}_1(t), \dot{u}_2(t))
\end{aligned} \tag{45}$$

$$\begin{aligned}
\ddot{u}_2(t) + \omega_2^2 u_2(t) &= -\zeta_{21} \dot{u}_1(t) - \zeta_{22} \dot{u}_2(t) \\
&- \frac{p_2 \rho U L D_B}{2M_2} \left(s_1 (p_1 \dot{u}_1(t) + p_2 \dot{u}_2(t)) - \frac{s_3 (p_1 \dot{u}_1(t) + p_2 \dot{u}_2(t))^3}{U^2} \right) \\
&- \frac{p_2}{M_2} \left[\frac{C_{e1} p_1 \dot{u}_1(t)}{\omega_1} + \frac{C_{e2} p_2 \dot{u}_2(t)}{\omega_2} + K_{e1} p_1 u_1(t) + K_{e2} p_2 u_2(t) \right] \\
&= f_2(u_1(t), u_2(t), \dot{u}_1(t), \dot{u}_2(t))
\end{aligned} \tag{46}$$

where $M_j = m_1 + p_j^2 m_2$, $\zeta_{jk} = \frac{c_1 - c_1(p_j + p_k) + (c_1 + c_2)p_j p_k}{M_j}$ ($j, k = 1, 2$). Assume the solutions of the modal coordinates $u_1(t)$ and $u_2(t)$ to be in the form as:

$$\begin{cases} u_1(t) = U_1 \cos(\omega_1 t - \varphi_1) \\ u_2(t) = U_2 \cos(\omega_2 t - \varphi_2) \end{cases} \tag{47}$$

According to the averaging method, neglecting the derivatives of U_i and φ_i , the derivatives of $u_1(t)$ and $u_2(t)$ are assumed to be:

$$\begin{cases} \dot{u}_1(t) = -U_1 \omega_1 \sin(\omega_1 t - \varphi_1) \\ \dot{u}_2(t) = -U_2 \omega_2 \sin(\omega_2 t - \varphi_2) \end{cases} \tag{48}$$

Substituting equations (47) and (48) into equations (45) and (46), then solving them simultaneously, we have:

$$\begin{cases} \dot{U}_1 = -\frac{1}{2\omega_1} \Phi_1 = -\frac{1}{2\pi\omega_1} \int_0^{2\pi} f_1(U_1, U_2, \varphi_1, \varphi_2) \sin \phi_1 d\phi_1 \\ \dot{\varphi}_1 = \frac{1}{2\omega_1 U_1} \Psi_1 = \frac{1}{2\pi\omega_1 U_1} \int_0^{2\pi} f_1(U_1, U_2, \varphi_1, \varphi_2) \cos \phi_1 d\phi_1 \\ \dot{U}_2 = -\frac{1}{2\omega_2} \Phi_2 = -\frac{1}{2\pi\omega_2} \int_0^{2\pi} f_2(U_1, U_2, \varphi_1, \varphi_2) \sin \phi_2 d\phi_2 \\ \dot{\varphi}_2 = \frac{1}{2\omega_2 U_2} \Psi_2 = \frac{1}{2\pi\omega_2 U_2} \int_0^{2\pi} f_2(U_1, U_2, \varphi_1, \varphi_2) \cos \phi_2 d\phi_2 \end{cases} \tag{49}$$

where $\begin{cases} \phi_1 = \omega_1 t - \varphi_1 \\ \phi_2 = \omega_2 t - \varphi_2 \end{cases}$. By introducing the following perturbation variables:

$$\begin{cases} \xi_1 = U_1 - U_{1s} \\ \eta_1 = \varphi_1 - \varphi_{1s} \\ \xi_2 = U_2 - U_{2s} \\ \eta_2 = \varphi_2 - \varphi_{2s} \end{cases} \tag{50}$$

The first-order approximation of equation (49) around the singularity point $(U_{1s}, \varphi_{1s}, U_{2s}, \varphi_{2s})$ can be obtained:

$$\begin{cases} 2\omega_1 \dot{\xi}_1 = - \left[\left(\frac{\partial \Phi_1}{\partial U_1} \right)_{U_1 = U_{1s}} \right] \xi_1 - \left[\left(\frac{\partial \Phi_1}{\partial \varphi_1} \right)_{\varphi_1 = \varphi_{1s}} \right] \eta_1 \\ - \left[\left(\frac{\partial \Phi_1}{\partial U_2} \right)_{U_2 = U_{2s}} \right] \xi_2 - \left[\left(\frac{\partial \Phi_1}{\partial \varphi_2} \right)_{\varphi_2 = \varphi_{2s}} \right] \eta_2 \\ 2\omega_1 \dot{\eta}_1 = \left[\frac{1}{U_1} \left(\frac{\partial \Psi_1}{\partial U_1} \right)_{U_1 = U_{1s}} - \frac{1}{U_1^2} \Psi_1 \right] \xi_1 \\ + \left[\frac{1}{U_1} \left(\frac{\partial \Psi_1}{\partial \varphi_1} \right)_{\varphi_1 = \varphi_{1s}} \right] \eta_1 + \left[\frac{1}{U_1} \left(\frac{\partial \Psi_1}{\partial U_2} \right)_{U_2 = U_{2s}} \right] \xi_2 \\ + \left[\frac{1}{U_1} \left(\frac{\partial \Psi_1}{\partial \varphi_2} \right)_{\varphi_1 = \varphi_{2s}} \right] \eta_2 \\ 2\omega_2 \dot{\xi}_2 = - \left[\left(\frac{\partial \Phi_2}{\partial U_1} \right)_{U_1 = U_{1s}} \right] \xi_1 - \left[\left(\frac{\partial \Phi_2}{\partial \varphi_1} \right)_{\varphi_1 = \varphi_{1s}} \right] \eta_1 \\ - \left[\left(\frac{\partial \Phi_2}{\partial U_2} \right)_{U_2 = U_{2s}} \right] \xi_2 - \left[\left(\frac{\partial \Phi_2}{\partial \varphi_2} \right)_{\varphi_2 = \varphi_{2s}} \right] \eta_2 \\ 2\omega_2 \dot{\eta}_2 = \left[\frac{1}{U_2} \left(\frac{\partial \Psi_2}{\partial U_1} \right)_{U_1 = U_{1s}} \right] \xi_1 + \left[\frac{1}{U_2} \left(\frac{\partial \Psi_2}{\partial \varphi_1} \right)_{\varphi_1 = \varphi_{1s}} \right] \eta_1 \\ + \left[\frac{1}{U_2} \left(\frac{\partial \Psi_2}{\partial U_2} \right)_{U_2 = U_{2s}} - \frac{1}{U_2^2} \Psi_2 \right] \xi_2 + \left[\frac{1}{U_2} \left(\frac{\partial \Psi_2}{\partial \varphi_2} \right)_{\varphi_1 = \varphi_{2s}} \right] \eta_2 \end{cases} \tag{51}$$

As equation (51) is in the state-space form that is, $\dot{\mathbf{X}} = \mathbf{A}\mathbf{X}$, using Lyapunov's second method, one can determine the stability of the singularity point $(U_{1s}, \varphi_{1s}, U_{2s}, \varphi_{2s})$. The solution is stable only if the eigenvalues of the corresponding Jacobian matrix of \mathbf{A} are negative real numbers. Otherwise, the singularity point corresponds to an unstable solution.

4. Mode activation mechanism

This section aims to investigate the solution characteristics of the 2DOF GPEH, that is, the conditions for the existence of multiple solutions and their stabilities. The system parameters of the 2DOF GPEH are listed in Table 1. The parameters of the primary oscillator and the attached piezoelectric transducer are determined from the experimental prototype in (Bibo et al., 2015). In the following study, the primary oscillator and the attached piezoelectric transducer remain unchanged. The mass and the damping ratio of the auxiliary oscillator are assumed the same as those of the primary oscillator by intentionally following the same assumption in (Lan et al., 2019). Hence, by comparing the results between the current work and (Lan et al., 2019), one could easily find that the difference between the analyses are originated from the different methods rather than the different system parameters. The stiffness of the auxiliary oscillator will be varied to explore its influence on the solution characteristics. In fact, varying either the stiffness or the mass of the auxiliary oscillator is essentially to alter its natural frequency, that is, $\omega_{10} = \sqrt{k_1/m_1}$. Hence, the actual purpose is to explore the influence of the natural frequency relationship

Table 1. System parameters of the 2DOF GPEH.

Mechanical parameters		Aerodynamic parameters	
Effective mass m_1 (g)	113.4	Air density, ρ (kg/m ³)	1.24
Effective mass m_2 (g)	113.4	Bluff body height, L (m)	0.1
Effective stiffness k_1 (N/m)	58.02	Cross flow dimension, D_B (m)	0.05
Effective stiffness k_2 (N/m)	58.02	Linear aerodynamic coefficient, s_1	2.5
Damping ratio ζ_1	0.003	Cubic aerodynamic coefficient, s_3	130
Damping ratio ζ_2	0.003	Load resistance R (Ω)	10 ¹²
Electromechanical coupling θ ($\mu\text{N/V}$)	190		
Capacitance C_p (nF)	187		

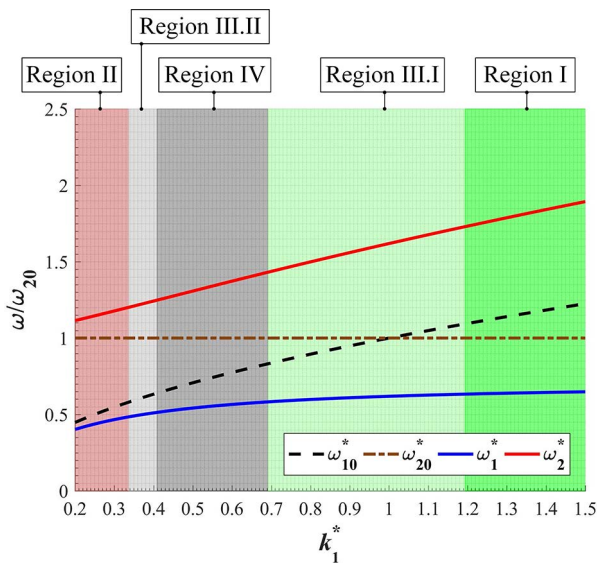


Figure 3. The relationship between the natural frequencies of the coupled 2DOF system (i.e. ω_2 and ω_1) and the natural frequencies of the primary and auxiliary oscillators (i.e. ω_{20} and ω_{10}). The red line represents ω_2 , the blue line represents ω_1 , the brown dash-dot line represents ω_{20} and the black dashed line represents ω_{10} . The colour shaded areas denote different regions having different solution characteristics.

between the primary and auxiliary oscillators on the solution characteristics.

By defining the non-dimensional stiffness of the auxiliary oscillator as $k_1^* = k_1/k_2$, we vary k_1^* from 0.2 to 1.5. Figure 3 shows the relationship between the natural frequencies of the coupled 2DOF system (i.e. ω_2 and ω_1) and the natural frequencies of the separated primary and auxiliary oscillators (i.e. ω_{20} and ω_{10}). As k_1^* varies, the solutions of the corresponding 2DOF GPEH are computed using the analytical method developed in the previous section.

According to the solution characteristics, the entire parametric space can be divided into five regions. Table 2 summarizes the solution characteristics in the five different regions. Note that the ‘Regions’ are named in a manner according to the characteristics of the solutions

rather than successively with k_1^* increasing from 0.2 to 1.5. In Region I, there exists only a single mathematically and physically achievable solution. This solution is stable and corresponds to a single-frequency LCO with the frequency of ω_1 . In Region II, there also exists only a single mathematically and physically achievable stable solution. But different from Region I, systems in Region II undergo single-frequency LCOs with the frequency of ω_2 . In Region III, there exist two mathematically but only one physically achievable solutions. To be more specific, Region III can be further classified into two sub-regions, namely, Region III.I and Region III.II. In Region III.I and Region III.II, either ω_1 or ω_2 related solutions are stable. Therefore, Region III.I and Region III.II are, respectively, similar to Region I and Region II from the physical point of view. In Region IV, all three solutions are mathematically achievable. However, the dual-frequency LCO solution is unstable. The other two single-frequency LCO solutions are stable. It is presumed that in Region IV, the system can optionally carry on the single-frequency LCO with the frequency of either ω_1 or ω_2 , depending on the initial condition. More detailed case studies of selected systems from different regions will be presented in the following section.

5. Equivalent circuit simulation

To verify the analytical solutions derived in section 3, an equivalent circuit model of the 2DOF GPEH is established based on the analogies between the dynamic equations of mechanical and electrical systems, which are intrinsically ordinary differential equations having exactly the same mathematical formulation. From the perspective of impedance analogy, the mechanical quantities of force and velocity are analogous to the electrical quantities of voltage and current, respectively. Consequently, the mass, spring and damper in the mechanical domain are severally represented as the inductor, capacitor and resistor in the electrical domain. It is worth noting that in the analogy between the spring and the capacitor, the capacitance of the capacitor equals to the compliance (i.e. the reciprocal of the

Table 2. Summary of solution characteristics of 2DOF GPEH in different regions.

	Region I	Region II	Region III.I	Region III.II	Region IV
k_1^* Ranges	[1.195, 1.5]	[0.2, 0.336]	[0.693, 1.194]	[0.337, 0.408]	[0.409, 0.692]
Representative cases	Case A $k_1^* = 1.4$	Case B $k_1^* = 0.3$	Case C $k_1^* = 0.8$	Case D $k_1^* = 0.36$	Case E $k_1^* = 0.5$
Single-frequency LCO (ω_1): $r_1(t) > 0; r_2(t) = 0$	Existent Stable	Non-existent NA	Existent Stable	Existent Unstable	Existent Stable
Single-frequency LCO (ω_2): $r_1(t) = 0; r_2(t) > 0$	Non-existent NA	Existent Stable	Existent Unstable	Existent Stable	Existent Stable
Dual-frequency LCO (ω_1 and ω_2): $r_1(t) > 0; r_2(t) > 0$	Non-existent NA	Non-existent NA	Non-existent NA	Non-existent NA	Existent Unstable
Number of mathematically achievable solutions	1	1	2	2	3
Number of physically achievable solutions	1	1	1	1	2

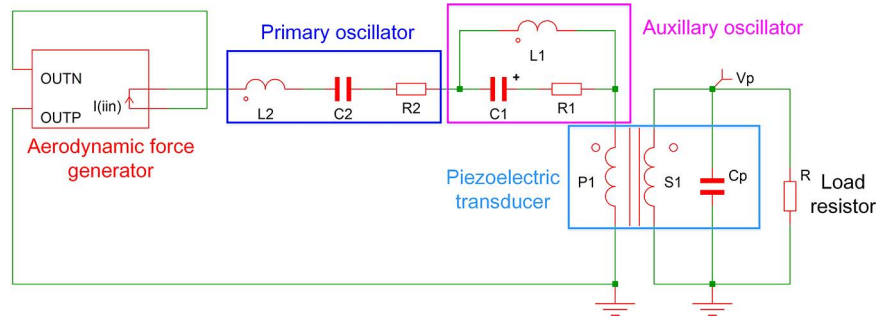


Figure 4. Equivalent circuit model of the 2DOF GPEH established in SIMetrix.

stiffness) of the spring. The piezoelectric transducer can be modelled as the combination of an ideal transformer and a capacitor, which describes its internal capacitance (Yang and Tang, 2009). The interface circuit can then be directly connected to the electrical equivalents of the mechanical components, through the coupling of the ideal transformer. The challenge of establishing the equivalent circuit model of the 2DOF GPEH lies in the representation of the nonlinear galloping-induced force. Fortunately, the nonlinear transfer function provided in the commercial circuit simulation software SIMetrix enables the users to define an arbitrary source as a function of variables of circuit components. Therefore, we can define a voltage source (i.e. the galloping-induced force) as the function of the current (i.e. velocity) through the inductor that represents the primary oscillator. Detailed procedure can be referred to the previous work in the literature (Tang et al., 2014; Wang et al., 2020b). Figure 4 shows the established equivalent circuit model of the 2DOF GPEH. A transient simulation should be conducted until the system converges to the steady-state. The voltage response across the load resistance R can then be directly measured by placing a voltage probe.

6. Case studies

In this section, example cases from different regions are considered in detail to give more in-depth insights into their dynamic characteristics. Case A, B, C, D and E are selected from Region I, II, III.I, III.II and IV, respectively. The system parameters, except the stiffness of the auxiliary oscillator, are the same as those listed in Table 1. k_1^* of the five cases are, severally, 1.4, 0.3, 0.8, 0.36 and 0.5, as declared in Table 2.

6.1. Case A from Region I

Case A is selected from Region I with $k_1^* = 1.4$. Under the open-circuit condition, the first and second natural frequencies of Case A can be calculated as 2.318 and 6.627 Hz, respectively. By increasing the wind speed, Figure 5(a) compares the voltage amplitudes predicted by the circuit simulation and the analytical method. The blue solid line denotes the voltage amplitude of the first harmonic component with the frequency of $f_1 = 2.318$ Hz, and the blue dashed line denotes the second harmonic component with the frequency of $f_2 = 6.627$ Hz. The black circles represent the circuit

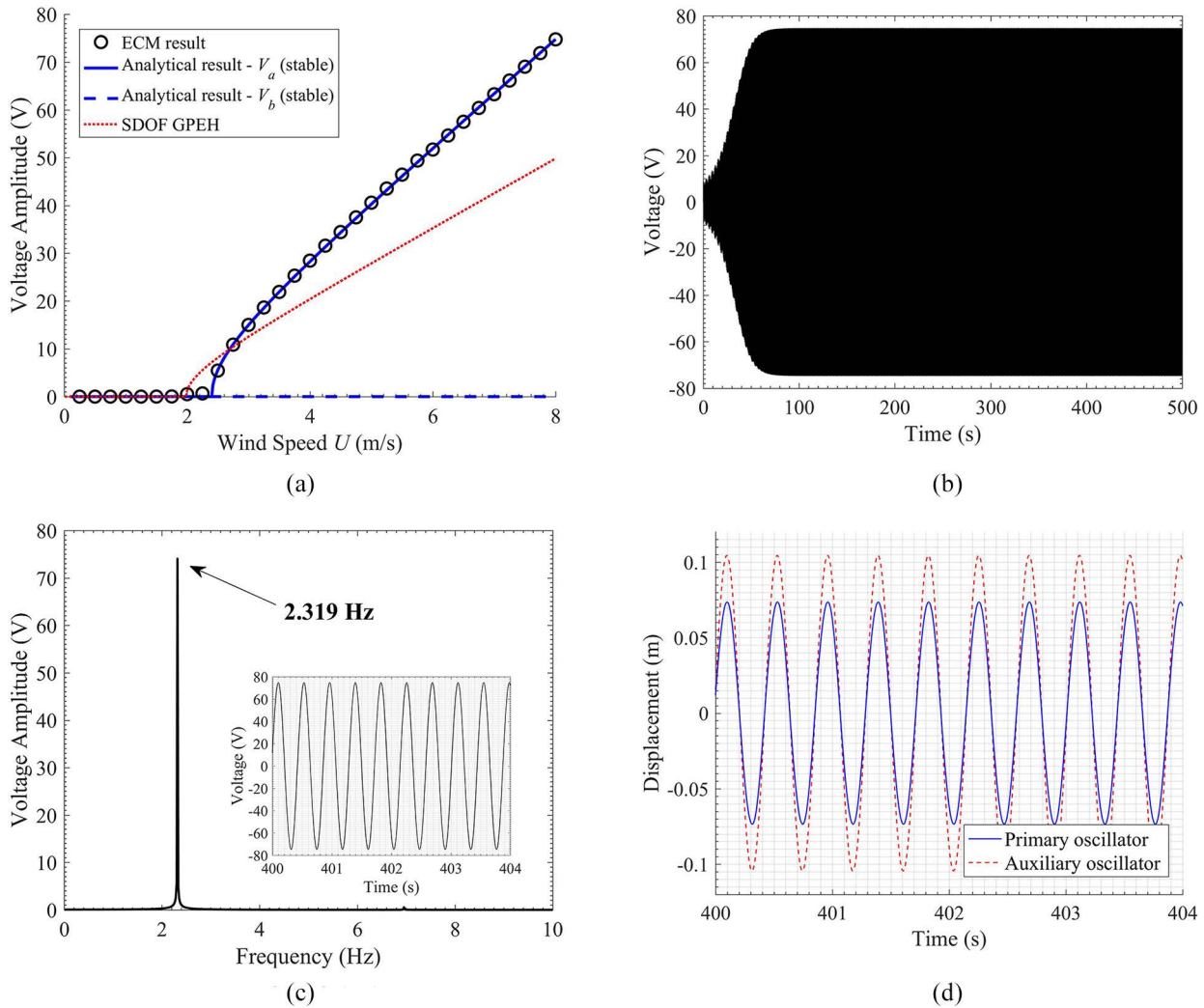


Figure 5. (a) Comparison of the voltage amplitudes versus wind speed obtained by the ECM method and the analytical method, (b) the transient voltage response at the wind speed of 8 m/s from circuit simulation, (c) the frequency spectrum of the steady-state response in (b), and (d) the steady-state responses of the displacements of the two oscillators. k_1^* of case A in Region I is 1.4.

simulation results. The analytically predicted response of the SDOF GPEH by removing the auxiliary oscillator is also provided for comparison. One can refer to (Lan et al., 2019) for the derivation of the analytical response of the SDOF GPEH. It is noted that the analytical result of the first harmonic component matches very well with the simulation result. The cut-in wind speed of the 2DOF GPEH is about 2.40 m/s. However, the blue dashed line is always zero, which indicates that the second mode vibration is not activated. Compared to the SDOF GPEH with a cut-in wind speed of 1.98 m/s, though the 2DOF GPEH is more difficult to be excited by the wind, the output voltage amplitude of the 2DOF GPEH is larger under a high-speed wind excitation. This prediction basically agrees with the experimental phenomenon reported in (Hu et al., 2021a).

To verify that the dynamic response in Case A is a single-frequency ($f_1 = 2.318$ Hz) limit cycle

oscillation, the transient response of the voltage output at the wind speed of 8 m/s is examined in Figure 5(b). The corresponding frequency spectrum of the steady-state response in Figure 5(b) is shown in Figure 5(c) using the Fast Fourier Transform (FFT) approach. It is clearly seen that only one peak with the amplitude of 74.75 V at the frequency near $f_1 = 2.318$ Hz is observed. Moreover, Figure 5(d) shows the steady-state in-phase motions of the displacements of the primary and the auxiliary oscillators, which tallies with the dynamic characteristic of the first mode vibration of a 2DOF system. Hence, it can be confirmed that only the first mode of the 2DOF GPEH is activated in Case A.

6.2. Case B from Region II

In Case B which falls into Region II, k_1^* is set to be 0.3. The first and the second natural frequencies of the

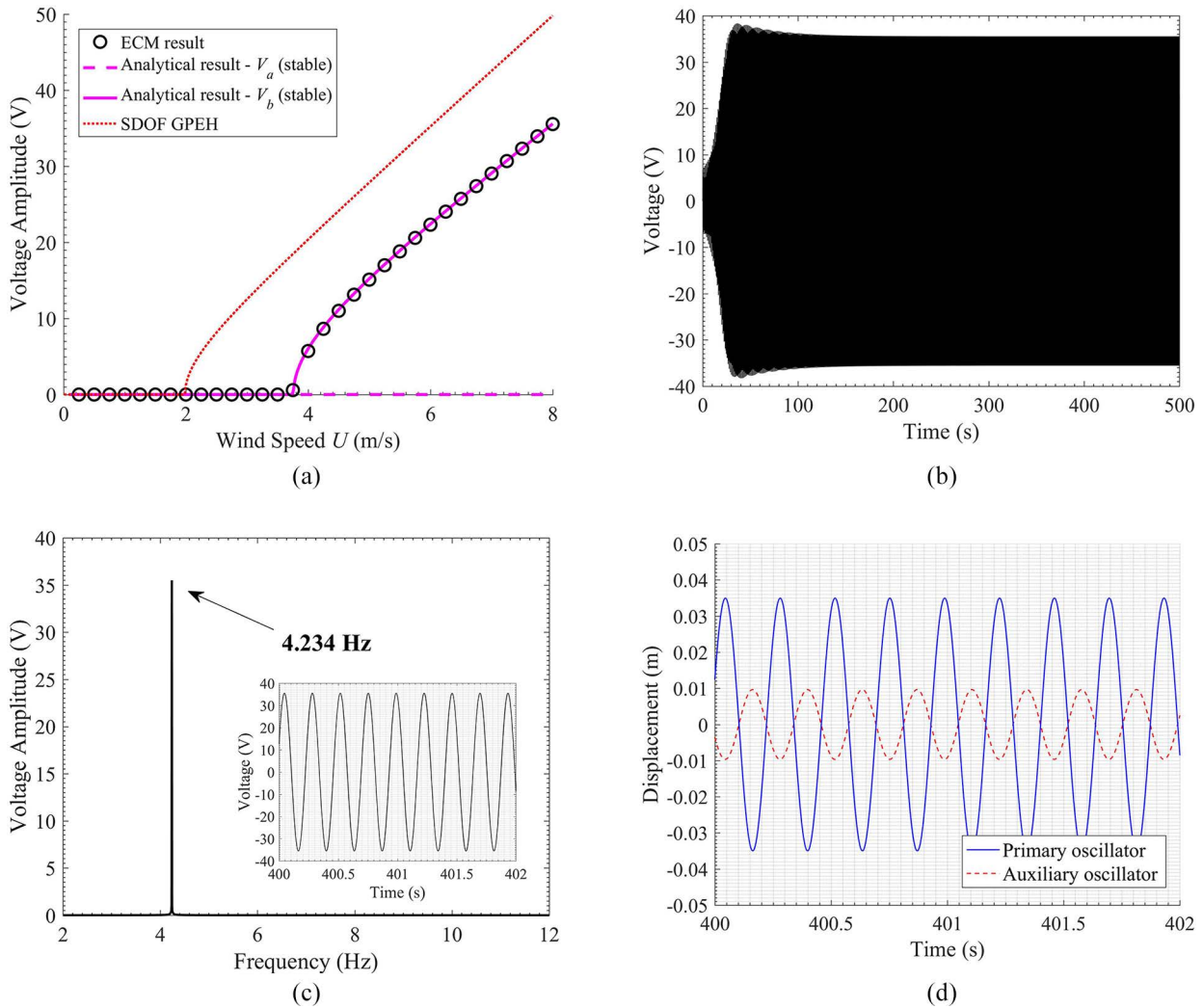


Figure 6. (a) Comparison of the voltage amplitudes versus wind speed obtained by the ECM method and the analytical method, (b) the transient voltage response at the wind speed of 8 m/s from circuit simulation, (c) the frequency spectrum of the steady-state response in (b), and (d) the steady-state responses of the displacements of the two oscillators. k_1^* of case B in Region II is 0.3.

2DOF GPEH, under the open-circuit condition, are 1.678 and 4.238 Hz, respectively. Figure 6(a) shows the voltage amplitude versus wind speed obtained from the circuit simulation and the analytical method. The pink solid and dashed lines represent the voltage amplitudes of the harmonic components with the frequencies of $f_2 = 4.238$ Hz and $f_1 = 1.678$ Hz, respectively. In contrast to Case A, it can be seen that the voltage amplitude of the first harmonic component with $f_1 = 1.678$ Hz is always zero, which indicates that the first mode vibration in Case B is inactivated. Nevertheless, the analytical result of the voltage amplitude of the second harmonic component with $f_2 = 4.238$ Hz overlaps the circuit simulation result. The cut-in wind speed is increased to 3.74 m/s. Compared

to the SDOF GPEH, the cut-in wind speed of the 2DOF GPEH is increased, and the output voltage amplitude is decreased.

To verify the mode activation, Figure 6(b) presents the transient response of the voltage output of Case B at the wind speed of 8 m/s. By performing the fast Fourier transform of the steady-state response in Figure 6(b), Figure 6(c) shows the corresponding frequency spectrum. As compared to Case A, the voltage amplitude of the 2DOF GPEH in Case B is reduced to 35.59 V. Moreover, it is clearly found that there is only a single peak at the frequency of 4.234 Hz, which is close to the second natural frequency of the 2DOF GPEH of Case B. Furthermore, from the steady-state responses of the displacements of the two oscillators as

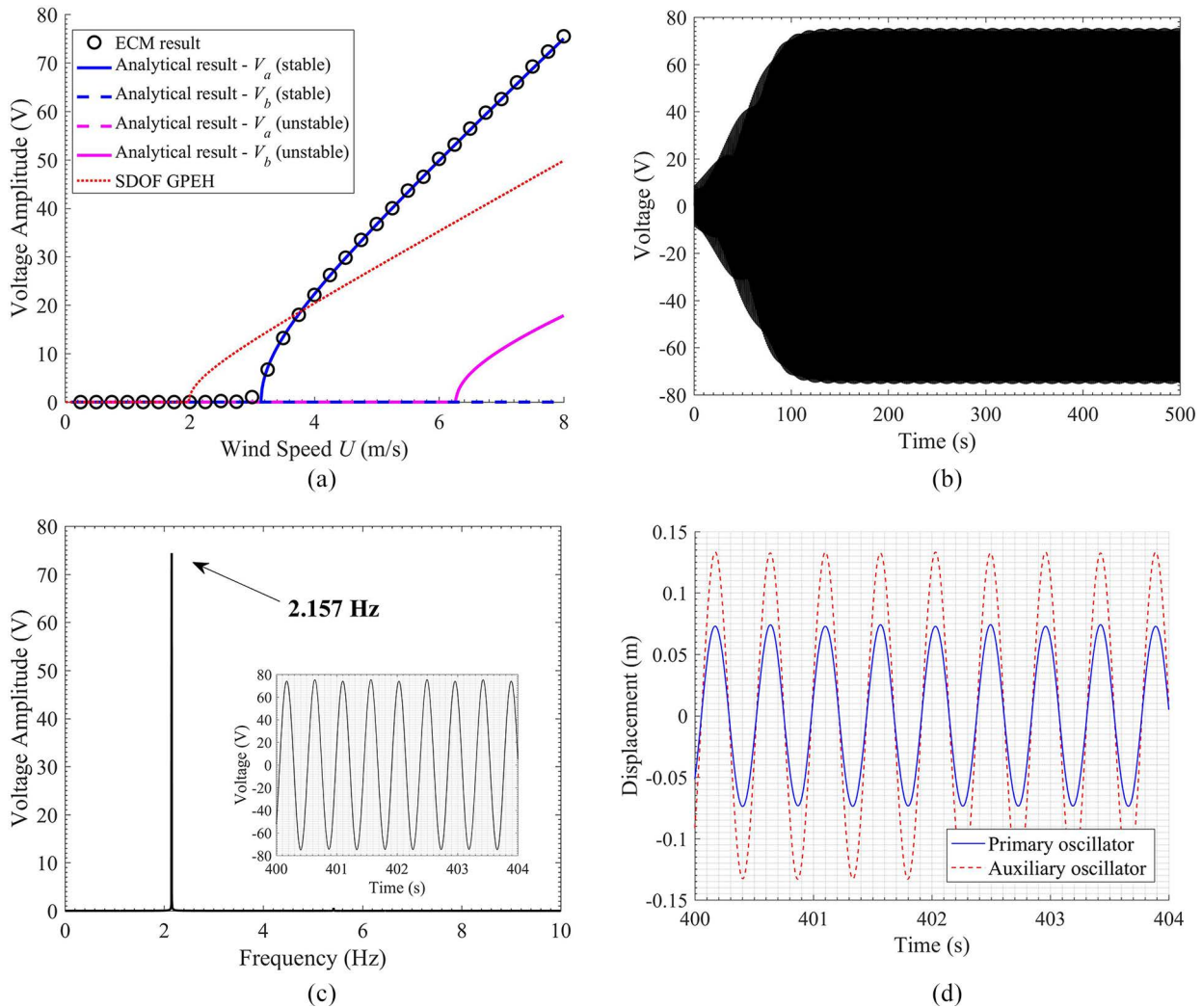


Figure 7. (a) Comparison of the voltage amplitudes versus wind speed obtained by the ECM method and the analytical method, (b) the transient voltage response at the wind speed of 8 m/s from circuit simulation, (c) the frequency spectrum of the steady-state response in (b), and (d) the steady-state responses of the displacements of the two oscillators. k_1^* of case C in Region III.I is 0.8.

illustrated in Figure 6(d), the out-of-phase motion also confirms the activation of the second mode vibration of the 2DOF GPEH in Case B.

6.3. Case C from Region III.I

k_1^* is set to be 0.8 in Case C to make it fall into Region III.I. The first two natural frequencies of the 2DOF GPEH consequently become 2.152 and 5.395 Hz, respectively. Figure 7(a) reveals the relationship between the voltage amplitude of the 2DOF GPEH and the wind speed. As mentioned in section 4, there exist two sets of solutions: one set of solution is stable, while the other one is unstable. The blue and pink lines represent the stable and unstable solutions, respectively. The solid and dashed lines denote non-zero and

zero values, respectively. For the stable solution, the first mode vibration is activated ($V_a \neq 0$) and the second mode vibration is inactivated ($V_b = 0$). In terms of the unstable solution, $V_a = 0$ while $V_b \neq 0$. In the circuit simulation, the initial condition is varied to explore the possibility of the existence of any solutions under different wind speeds. However, from Figure 7(a), it is noted that the circuit simulation result matches only with the analytical result of the voltage amplitude V_a related to the harmonic component having the frequency of $f_1 = 2.152$ Hz. It indicates that only the stable solution can be physically achieved. The stabilities of the solutions are thus verified. According to the branch of the stable solution, the cut-in wind speed is 3.14 m/s. Compared to the SDOF GPEH, it can be found that 2DOF GPEH produces a larger

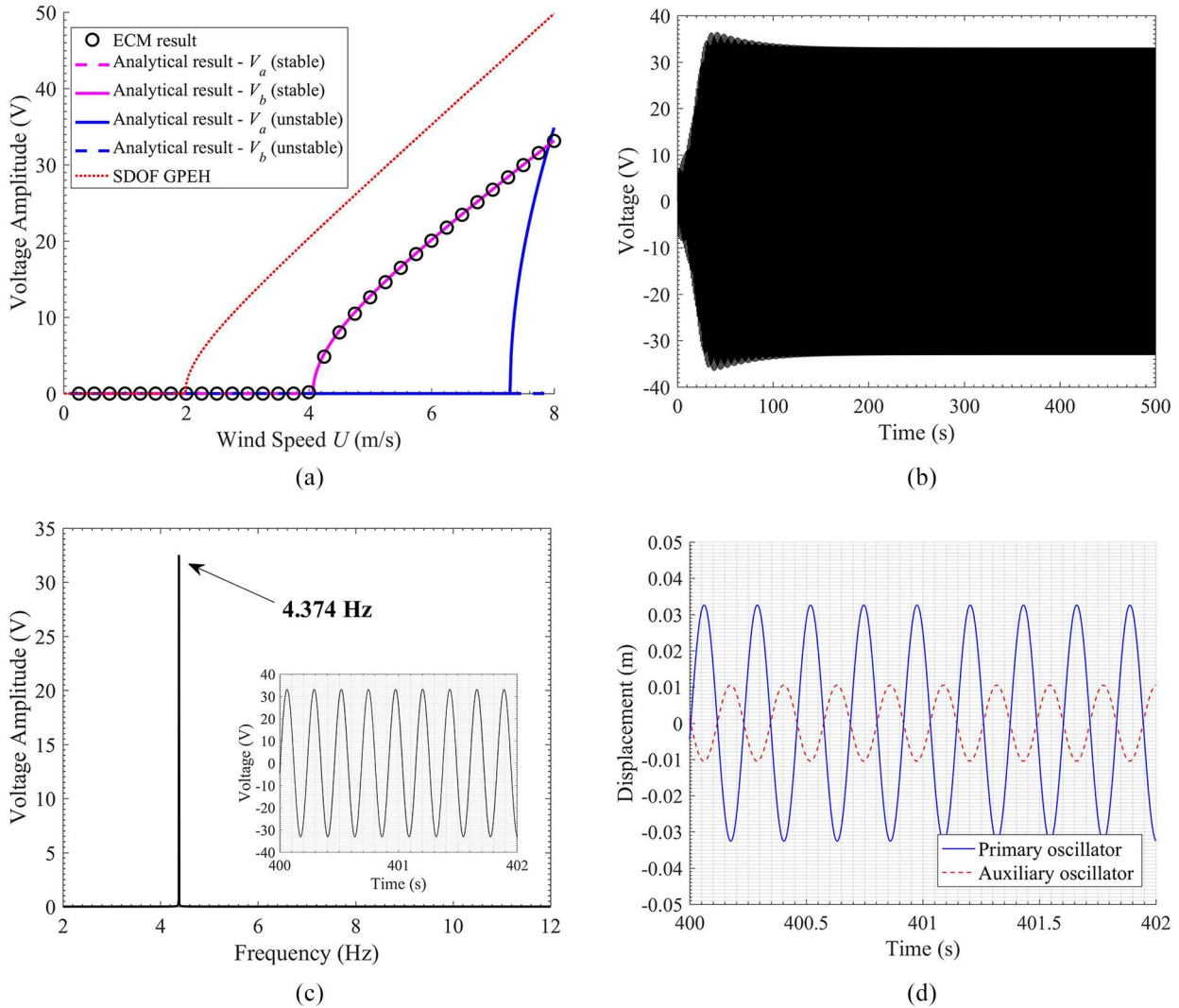


Figure 8. (a) Comparison of the voltage amplitudes versus wind speed obtained by the ECM method and the analytical method, (b) the transient voltage response at the wind speed of 8 m/s from circuit simulation, (c) the frequency spectrum of the steady-state response in (b), and (d) the steady-state responses of the displacements of the two oscillators. k_1^* of case D in Region III.II is 0.36.

output voltage amplitude when both of them are excited under a relatively high wind speed.

The transient voltage response of the 2DOF GPEH at the wind speed of 8 m/s in Case C is plotted in Figure 7(b). The corresponding frequency spectrum of the steady-state response is presented in Figure 7(c). The voltage amplitude is 74.94 V and the dominant frequency is 2.157 Hz, which is close to the first natural frequency of the 2DOF GPEH. Figure 7(d) further shows the steady-state responses of the displacements of the two oscillators. Both the spectral analysis result presented in Figure 7(c) and the in-phase motion characteristic revealed in Figure 7(d) validate the activation of the first mode vibration of the 2DOF GPEH in Case C from Region III.I. As compared to the results in section 6.1, one may have noticed that only from the circuit simulation phenomenon, it is actually difficult to distinguish the difference between Case A from Region

I and Case C from Region III.I. The analytical method helps develop a thorough understanding of the mechanisms behind them.

6.4. Case D from Region III.II

A representative Case D from Region III.II is achieved by setting k_1^* to be 0.36. The first two natural frequencies of the 2DOF GPEH of Case D are, respectively, 1.779 Hz and 4.378 Hz. As aforementioned in section 4, systems that fall into Region III.II also have two sets of periodic solutions. Figure 8(a) shows the two sets of analytical solutions and the circuit simulation result of the voltage amplitude under different wind speeds. To keep consistency, lines with different colours represent different sets of solutions: pink colour – stable solutions, blue colour – unstable solutions. The solid and dashed lines, respectively, represent non-zero and zero

solutions as before. In contrast to Case C from Region III.I, the simulation result only agrees with the analytical result of the V_b from the set of the stable solution, which implies the activation of the second mode vibration of the 2DOF GPEH. Though the initial condition is varied, the simulation result converges to only the stable solution that is analytically obtained. Moreover, by looking at the stable solution, it is noted that the cut-in wind speed of the 2DOF GPEH in Case D is 4.06 m/s. Compared to the SDOF GPEH, the performance of the 2DOF GPEH is reduced to the absolute inferiority: the cut-in wind speed is increased, and the output voltage amplitude is decreased.

The transient voltage response of the 2DOF GPEH of Case D under the wind speed of 8 m/s and the corresponding frequency spectral analysis result of the steady-state response are presented in Figure 8(b) and (c), respectively. A single peak with the amplitude of 33.12 V around the frequency that is close to the second natural frequency of the 2DOF GPEH is observed in Figure 8(c), indicating the activation of the second mode vibration. Moreover, the out-of-phase steady-state responses of the displacements of the two oscillators presented in Figure 8(d) provide further verification. In fact, as the relationship between Case A from Region I and C from Region III.I, the difference between Case D from Region III.II and Case B from Region II can not be detected only based on the circuit simulation results as well. With the help of the analytical method, the underlying mechanisms and differences behind the two cases are unveiled.

6.5. Case E from Region IV

Finally, Case E with k_1^* of 0.36 that belongs to Region IV is investigated. The first two natural frequencies of the 2DOF GPEH in Case E are 1.950 and 4.707 Hz, respectively. The relationship between the voltage amplitude and the wind speed for Case E, as illustrated in Figure 9(a), becomes more complicated than the previous cases due to the existence of three sets of solutions as aforementioned in section 4. The lines with blue and pink colours indicate stable solutions, and the green colour indicates unstable solutions. The solid and dashed lines represent non-zero and zero stable solutions. The dotted and dash-dot lines denote the unstable solutions of V_a and V_b , respectively. The initial condition of the 2DOF GPEH is varied to capture any possible solutions. From Figure 9(a), it can be seen that the simulation result splits into two branches after exceeding the cut-in wind speeds. It is worth noting that the starting points (i.e. the cut-in wind speeds) of the two branches are slightly different as 4.78 m/s (pink branch) and 4.80 m/s (blue branch), respectively. Each branch of the simulation result matches with each set

of stable solutions. No numerical solutions can be found along the green lines which are unstable solutions. Hence, the numerical result verifies the stabilities of the solutions determined using the method presented in 3.3. The blue branch is characterized by non-zero V_a and constantly zero V_b , which indicates the activation of the first mode vibration of the 2DOF GPEH. The pink branch is characterized by non-zero V_b but constantly zero V_a , which implies the activation of the second mode vibration of the 2DOF GPEH. Since the amplitude of the blue branch is always larger than that of the pink branch under the same wind speed, the blue and the pink branches are hereinafter termed as high-energy and low-energy orbits, respectively. According to the theories of nonlinear dynamics, whether the steady-state response of the 2DOF GPEH eventually converges to the high-energy or the low-energy orbit normally depends on the initial condition. Compared to the SDOF GPEH, the cut-in wind speed of the 2DOF GPEH is increased no matter from the point of view of the high-energy or the low-energy orbit solution. The low-energy orbit solution is in an absolute inferior position, since its amplitude is always smaller than that of the SDOF GPEH. However, when the high-energy orbit is activated, the 2DOF GPEH could produce a larger voltage output than the SDOF GPEH if the wind speed is sufficiently large.

By setting the initial velocity of the auxiliary oscillator as 3 m/s, while keeping other initial values (i.e. the initial displacement and velocity of the primary oscillator and the initial displacement of the auxiliary oscillator) to be zeros, Figure 9(b) and (c) show the transient voltage response of the 2DOF GPEH under the wind speed of 8 m/s and the corresponding frequency spectrum of the steady-state part, respectively. The steady-state voltage amplitude is 67.35 V, and the dominant frequency is 1.952 Hz, which is close to the first natural frequency of the 2DOF GPEH. The spectral analysis result can be deemed as a direct evidence that the first mode vibration of the 2DOF GPEH is activated. Besides that, the activation of the first mode vibration can also be identified from the in-phase motions of the two oscillators revealed in Figure 9(d).

Subsequently, the initial velocity of the auxiliary oscillator is reduced to 0.5 m/s, while the other initial values are kept the same as zeros. The transient voltage response and the spectral analysis result of the corresponding steady-state part are presented in Figure 10(a) and (b), respectively. Different from the previous result in Figure 9(b) and (c), the steady-state voltage amplitude decreases to 27.80 V and the dominant frequency increases to 4.704 Hz which becomes close to the second natural frequency of the 2DOF GPEH. The spectral analysis result indicates that the second mode vibration of the 2DOF GPEH is activated after

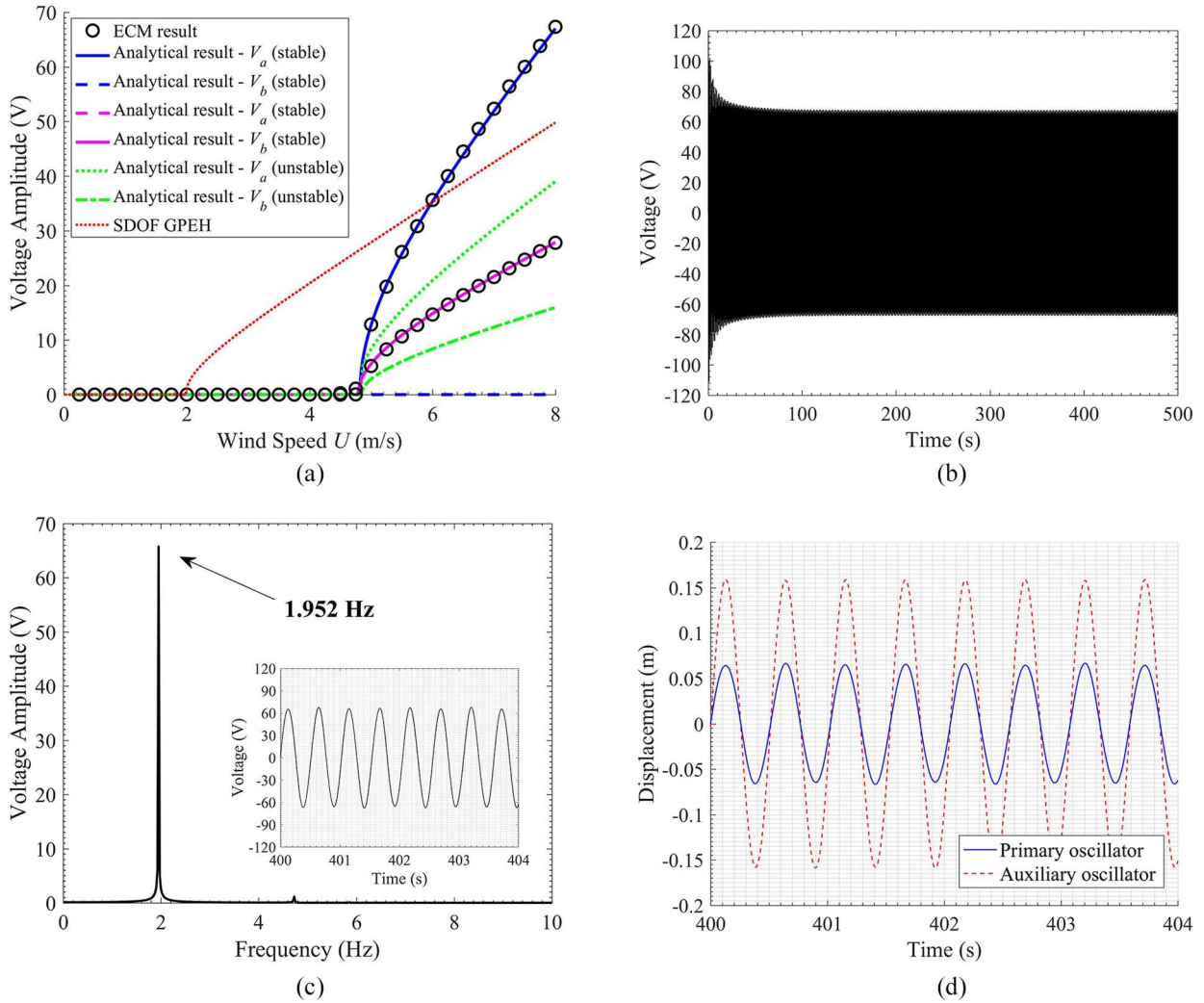


Figure 9. (a) Comparison of the voltage amplitudes versus wind speed obtained by the ECM method and the analytical method, (b) the transient voltage response at the wind speed of 8 m/s from circuit simulation, the initial velocity of the auxiliary oscillator is 3 m/s, (c) the frequency spectrum of the steady-state response in (b), and (d) the steady-state responses of the displacements of the two oscillators. k_1^* of case E in Region IV is 0.5.

changing the initial condition. In addition, the transient displacement responses of the two oscillators, presented in Figure 9(d), provide a further verification.

From the above analyses, it is noted that the activation of the first mode could benefit energy harvesting. In contrast, the activation of the second mode always deteriorates the energy harvesting performance. To give a more vivid but qualitative explanation, the modal shapes of the 2DOF GPEH associated with the first two resonant frequencies are plotted in Figure 11. It should be noted that the above theoretical analyses are based on a lumped parameter model. The following modal analysis is performed base on the beam structure model proposed in (Hu et al., 2021a) to provide a better graphic demonstration. The yellow arrows denote positive displacements. The red arrows denote negative displacements. When the first mode is activated, as shown in Figure 11(a), it can be seen that the motions

of the primary oscillator (i.e. represented by the bluff body) and the auxiliary oscillator (i.e. represented by the tip mass of the parasitic beam) are in phase, that is, always in the same direction. Moreover, the displacement amplitude of the auxiliary oscillator is relatively larger than that of the primary oscillator. Thus, it can be deduced that the reaction force applied on the primary oscillator by the auxiliary oscillator is in-phase with the motion of the primary oscillator, playing the role of promoting the vibration of the primary oscillator. As the piezoelectric transducer (marked in cyan) is attached to the host beam, that is, coupled with the primary oscillator, the voltage output from the transducer is unsurprisingly increased.

However, when the second mode is activated, as shown in Figure 11(b), the situation becomes different. The motion of the auxiliary oscillator becomes out-of-phase with the motion of the primary oscillator: the

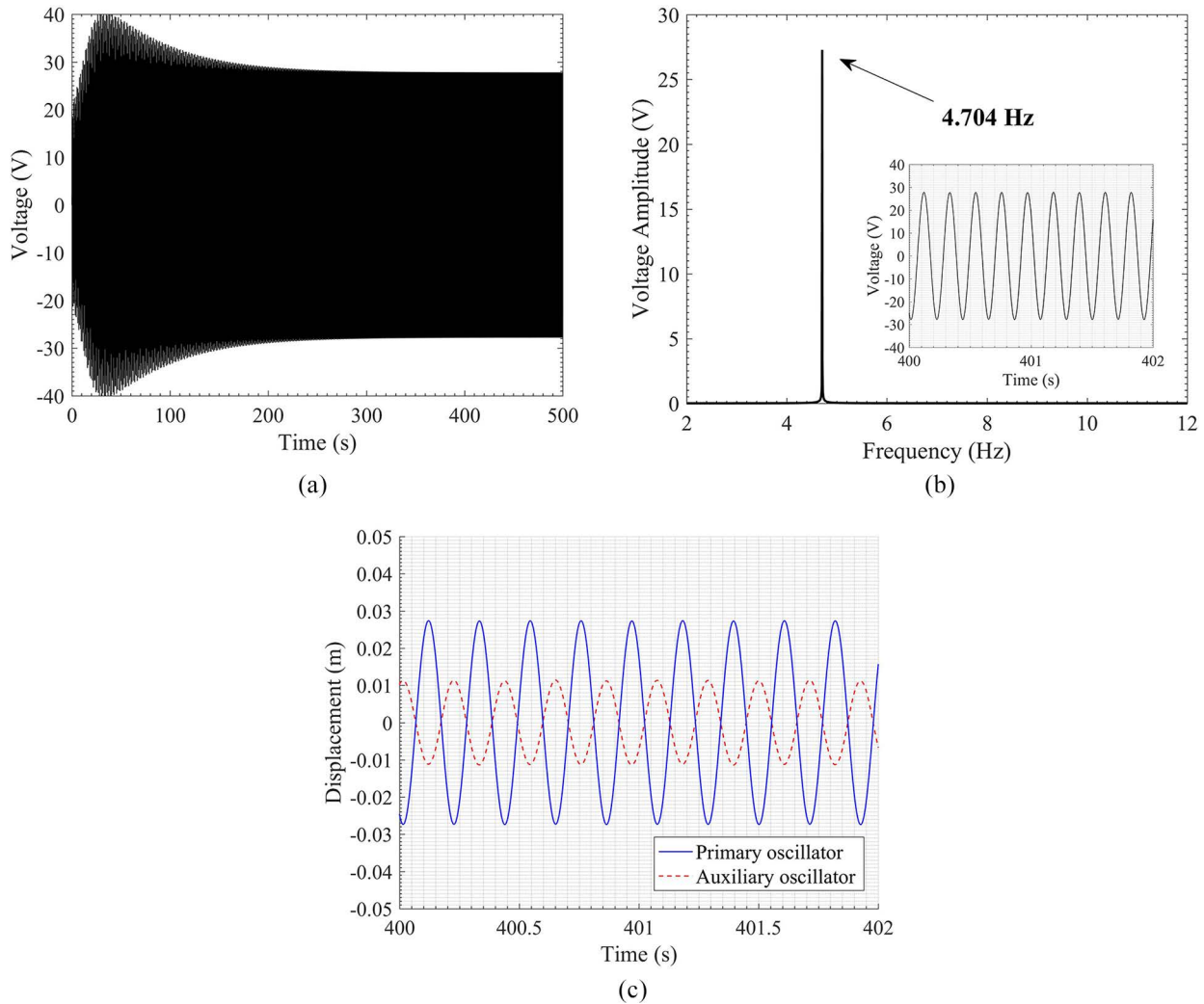


Figure 10. (a) The transient voltage response at the wind speed of 8 m/s from circuit simulation, the initial velocity of the auxiliary oscillator is 0.5 m/s, (b) the frequency spectrum of the steady-state response in (a), and (c) the steady-state responses of the displacements of the two oscillators. k_1^* of case E in Region IV is 0.5.

yellow and red arrows denote opposite displacement directions. Hence, the reaction force applied on the primary oscillator by the auxiliary becomes a resistance force. The vibration amplitude of the primary oscillator is, thus, decreased, as well as the output voltage amplitude produced by the attached piezoelectric transducer.

7. Design guidelines

Cut-in wind speed and output voltage amplitude are the two figures of merit to evaluate the performance of a galloping energy harvester. In different situations, different vibration modes of the 2DOF GPEH may be activated. The cut-in wind speeds for different situations are actually different. By forcing the response amplitudes $r_1(t)$ and $r_2(t)$ in equations (37) and (38) to be zero, respectively, one obtains the cut-in wind speed for different situations.

$$U_{cr1} = \frac{2P_1 c_1 \omega_1 - 2Q_1 k_1 - 2(c_1 + c_2)\omega_1 - 2C_{e1}}{D_B L \rho s_1 \omega_1} \quad (52)$$

$$U_{cr2} = \frac{2J_1 c_1 \omega_2 - 2K_1 k_1 - 2(c_1 + c_2)\omega_2 - 2C_{e2}}{D_B L \rho s_1 \omega_2} \quad (53)$$

Since in Region I and III.I, there exists only a single stable solution of the limit cycle oscillation with the frequency of ω_1 , equation (52) should be adopted to compute the cut-in wind speed. For a similar reason, equation (53) should be used to predict the cut-in wind speed in Region II and III.II. In Region IV, as two stable solutions co-exist and each corresponds to the limit cycle oscillation with the frequency of ω_1 and ω_2 , respectively, the two cut-in wind speeds computed by equations (52) and (53) should simultaneously exist. It is worth mentioning that Abdelmoula and Abdelkafi (2016) derived the cut-in wind of a SDOF GPEH through analysing the stability of the equilibrium point.

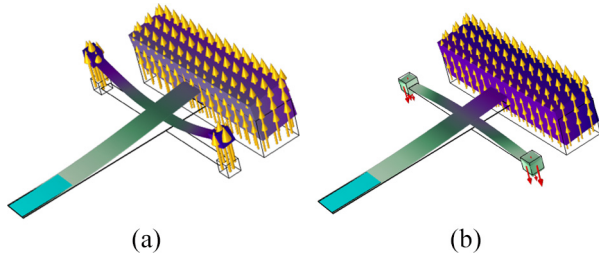


Figure 11. Finite element simulation obtained: (a) first modal shape, (b) second modal shape of the 2DOF GPEH studied in (Hu et al., 2021a). The yellow arrows denote positive displacements, and the red arrows denote negative displacements.

When the equilibrium point becomes unstable, it indicates that the SDOF GPEH starts to oscillate and produce considerable energy output. The critical condition for the equilibrium point turns into unstable from stable yields the cut-in wind speed.

Using the above two formulas (i.e. equations (52) and (53)), for the given system with the parameters listed in Table 1, Figure 12 shows the effect of k_1^* on the cut-in wind speed of the 2DOF GPEH. It can be found that with the increase of k_1^* , the cut-in wind speed U_{cr1} monotonously decreases, while the cut-in wind speed U_{cr2} monotonously increases. Moreover, when the system falls into Region I and III.I, the cut-in wind speed U_{cr1} is always smaller than that (i.e. U_{cr2}) when the system falls into Region II and III.II, except near the left fringe of Region III.I. It indicates that systems in Region I and III.I are more suitable for the application of low-wind speed energy harvesting. Besides that, in Region IV, the cut-in wind speeds U_{cr1} and U_{cr2} co-exist, and both reach a high level because of the monotone properties of them. Therefore, for the purpose of low-wind speed energy harvesting, one

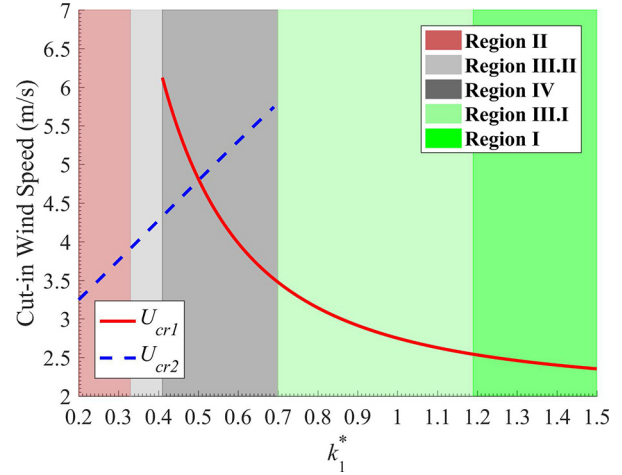


Figure 12. Effect of k_1^* on the cut-in wind speed of the 2DOF GPEH.

should avoid designing a 2DOF GPEH that falls into Region IV as well.

To investigate the evolution of the voltage amplitude with respect to the change of k_1^* , Figure 13 shows the corresponding results. Note that in Region IV, two stable solutions co-exist: one refers to the high-energy orbit with a larger amplitude, and the other one refers to the low-energy orbit with a smaller amplitude. Figure 13(a) and (b) present the results containing the high-energy and low-energy orbit solutions, respectively. The data in most areas of both Figure 13(a) and (b) coincide with each other, except in the narrow area of Region IV, which corresponds to a multiple solution region. It can be seen that when k_1^* exceeds Region IV and enters Region III.I and I, the output voltage amplitude becomes significantly large. However, when k_1^* is small and falls into Region II and III.II, the output voltage amplitude is dramatically reduced. In Region IV,

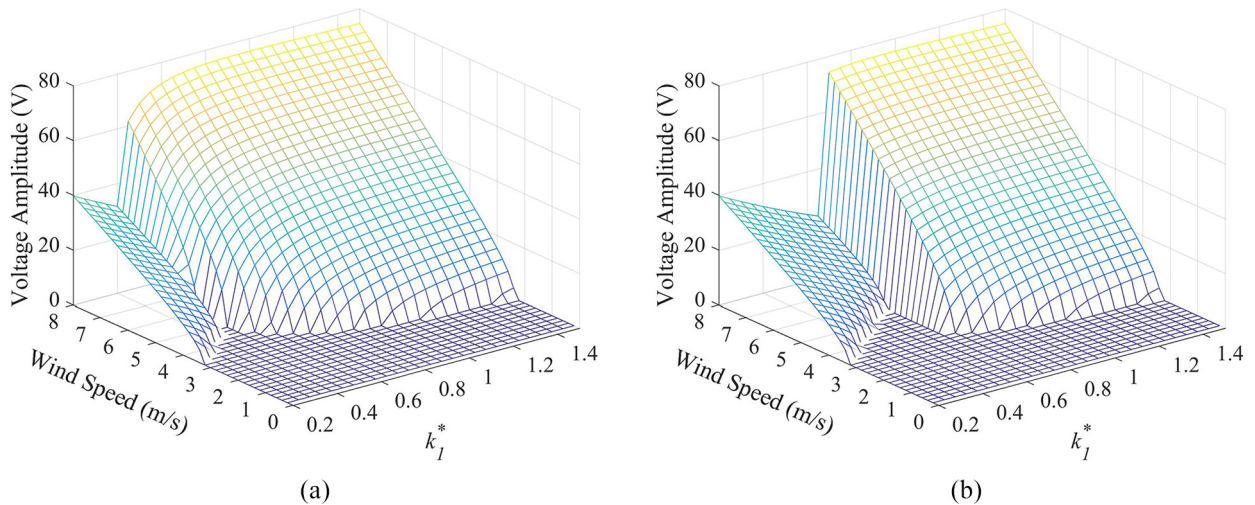


Figure 13. Voltage amplitude versus the wind speed and k_1^* : (a) the high-energy orbit and (b) the low-energy orbit.

the system can converge to different solutions depending on the initial condition. Though when the high-energy orbit is triggered in Region IV, the output voltage amplitude is comparable with that in Region I and III.I. Considering the uncertainty of the dynamic behaviour in Region IV, systems are not recommended to be designed within this area. On the other hand, from Figure 13, we can also note that the cut-in wind speed is relatively low when the system falls into Region III.I and I, which is in consistency with the analysis of Figure 12.

In brief summary, from both perspectives of lowering down cut-in wind speed and enlarging voltage output, the parameters of the 2DOF GPEH studied in this research should be tuned to make it fall into Region I or III.I to guarantee desirable predicatable energy harvesting performance.

8. Conclusions

This paper has presented a thorough study of a 2DOF galloping-based energy harvester. A theoretical model has been developed and analytical solutions have been derived. According to the analysis of the solution characteristics, the design space is divided into five regions featured with different dynamic behaviours, which have been comprehensively investigated.

- (a) In Region I and II, there exists only a single stable solution, and the 2DOF GPEH exhibits a single-frequency limit cycle oscillation. The difference between them is that the frequencies of the limit cycle oscillations in Region I and II, are the first and second natural frequencies of the 2DOF GPEH, respectively. Hence, the first and the second mode vibrations are activated, respectively, in Region I and II.
- (b) Systems in Region III.I and III.II have two solutions: one is stable, and the other is unstable. The stable solutions in Region III.I and III.II are, respectively, the first and the second vibration mode related limit cycle oscillations. Therefore, by considering only the stable solutions, Region III.I and III.II are, respectively, similar to Region I and II.
- (c) For Region IV, there exist three solutions. However, only two of them are stable. One stable solution corresponds to the single-frequency limit cycle oscillation around the first natural frequency. The other stable solution corresponds to the single-frequency limit cycle oscillation around the second natural frequency. Depending on the initial condition, the systems in Region IV may converge to the limit cycle oscillation around the first or the second natural frequency.

An equivalent circuit model has been established to verify the theoretical model and confirm the dynamic behaviours of the 2DOF GPEH in different regions. From the perspective of reducing the cut-in wind speed and increasing the output voltage amplitude, the first mode vibration of the 2DOF GPEH is preferred to be activated. Based on the theoretical analysis, several design guidelines are provided to guarantee a sound energy harvesting performance of the 2DOF GPEH under investigation in this study. First, systems should not be designed in Region II and III.II, where only the second mode limit cycle oscillation can be incurred. Second, Region IV should also be evaded, due to the uncertainty of mode activation, that is, convergence to high-energy or low-energy orbits is indeterminate. Third, the stiffness of the auxiliary oscillator should be tuned relatively large, since the cut-in wind speed reduces, and the output voltage amplitude increases with the increase of the stiffness of the auxiliary oscillator.

Declaration of conflicting interests

The author(s) declared no potential conflicts of interest with respect to the research, authorship and/or publication of this article.

Funding

The author(s) disclosed receipt of the following financial support for the research, authorship and/or publication of this article: This work was supported by the National Natural Science Foundation of China (Grant No.: 51977196), and China Postdoctoral Science Foundation (2020T130557).

ORCID iDs

Junrui Liang  <https://orcid.org/0000-0003-2685-5587>
Lihua Tang  <https://orcid.org/0000-0001-9031-4190>

References

- Abdelkefi A (2016) Aeroelastic energy harvesting: A review. *International Journal of Engineering Science* 100: 112–135.
- Abdelkefi A, Hajj MR and Nayfeh AH (2012) Power harvesting from transverse galloping of square cylinder. *Nonlinear Dynamics* 70(2): 1355–1363.
- Abdelmoula H and Abdelkefi A (2016) The potential of electrical impedance on the performance of galloping systems for energy harvesting and control applications. *Journal of Sound and Vibration* 370: 191–208.
- Alhadidi AH, Abderrahmane H and Daqaq MF (2016) Exploiting stiffness nonlinearities to improve flow energy capture from the wake of a bluff body. *Physica D: Nonlinear Phenomena* 337: 30–42.
- Ali M, Arafa M and Elaraby M (2013) Harvesting energy from galloping oscillations. In: *Proceedings of the World*

- Congress on Engineering*, London, UK, 3–5 July. London, UK: WCE.
- Barrero-Gil A, Alonso G and Sanz-Andres A (2010) Energy harvesting from transverse galloping. *Journal of Sound and Vibration* 329(14): 2873–2883.
- Bibo A, Alhadidi AH and Daqaq MF (2015) Exploiting a nonlinear restoring force to improve the performance of flow energy harvesters. *Journal of Applied Physics* 117(4): 045103.
- Blevins R and Iwan W (1974) The galloping response of a two-degree-of-freedom system. *Journal of Applied Mechanics* 41(4): 1113–1118.
- Bryant M and Garcia E (2011) Modeling and testing of a novel aeroelastic flutter energy harvester. *Journal of Vibration and Acoustics* 133(1): 011010.
- Desai Y, Shah A and Popplewell N (1990) Galloping analysis for two-degree-of-freedom oscillator. *Journal of Engineering Mechanics* 116(12): 2583–2602.
- Erturk A and Inman DJ (2008) On mechanical modeling of cantilevered piezoelectric vibration energy harvesters. *Journal of Intelligent Material Systems and Structures* 19(11): 1311–1325.
- Eugeni M, Elahi H, Fune F, et al. (2020) Numerical and experimental investigation of piezoelectric energy harvester based on flag-flutter. *Aerospace Science and Technology* 97: 105634.
- Ewerc F, Wang G and Cain B (2014) Experimental investigation of galloping piezoelectric energy harvesters with square bluff bodies. *Smart Materials and Structures* 23(10): 104012.
- Fang S, Fu X, Du X, et al. (2019) A music-box-like extended rotational plucking energy harvester with multiple piezoelectric cantilevers. *Applied Physics Letters* 114(23): 233902.
- Hu G, Tang L, Liang J, et al. (2019) Modelling of a cantilevered energy harvester with partial piezoelectric coverage and shunted to practical interface circuits. *Journal of Intelligent Material Systems and Structures* 30(13), 1045389X19849269.
- Hu G, Tang L and Yang Y (2020) A Lumped Parameter Approach for Analysing a Metamaterial Beam Based Piezoelectric Energy Harvester around Fundamental Resonance. In: *ASME Conference on Smart Materials, Adaptive Structures and Intelligent Systems (SMASIS)*, Irvine, CA, USA, 15 September (Virtual Conference). Irvine, CA: American Society of Mechanical Engineers Digital Collection.
- Hu G, Wang J, Qiao H, et al. (2021a). An experimental study of a two-degree-of-freedom galloping energy harvester. *International Journal of Energy Research* 45(2): 3365–3374.
- Hu G, Wang J and Tang L (2021b) A comb-like beam based piezoelectric system for galloping energy harvesting. *Mechanical Systems and Signal Processing* 150: 107301.
- Hu G, Wang J, Su Z, et al. (2019) Performance evaluation of twin piezoelectric wind energy harvesters under mutual interference. *Applied Physics Letters* 115(7): 073901.
- Hu G, Zhao B, Tang L, et al. (2018) Modeling of Cantilevered Piezoelectric Energy Harvester with Standard DC Interface Circuit. In: *International Conference on Noise and Vibration Engineering*, Leuven, Belgium, 17–19 September. Leuven, Belgium.
- Javed U, Abdelkefi A and Akhtar I (2016) An improved stability characterization for aeroelastic energy harvesting applications. *Communications in Nonlinear Science and Numerical Simulation* 36: 252–265.
- Jo S-H, Yoon H, Shin YC, et al. (2020) An analytical model of a phononic crystal with a piezoelectric defect for energy harvesting using an electroelastically coupled transfer matrix. *International Journal of Mechanical Sciences* 193: 106160.
- Lan C, Tang L, Hu G, et al. (2019) Dynamics and performance of a two degree-of-freedom galloping-based piezoelectric energy harvester. *Smart Materials and Structures* 28(4): 045018.
- Liu F-R, Zhang W-M, Zhao L-C, et al. (2020) Performance enhancement of wind energy harvester utilizing wake flow induced by double upstream flat-plates. *Applied Energy* 257: 114034.
- Luongo A and Di Fabio F (1993) Multimodal galloping of dense spectra structures. *Journal of Wind Engineering and Industrial Aerodynamics* 48(2–3): 163–174.
- Naseer R, Dai H, Abdelkefi A, et al. (2017) Piezomagnetoelastic energy harvesting from vortex-induced vibrations using monostable characteristics. *Applied Energy* 203: 142–153.
- Priya S and Inman DJ (2009) *Energy Harvesting Technologies*, vol. 21. New York, NY: Springer.
- Rudowski J (1982) Limit cycles in self-excited multi-degree-of-freedom systems. *Journal of Sound and Vibration* 81(1): 33–49.
- Sirohi J and Mahadik R (2011) Piezoelectric wind energy harvester for low-power sensors. *Journal of Intelligent Material Systems and Structures* 22(18): 2215–2228.
- Sirohi J and Mahadik R (2012) Harvesting wind energy using a galloping piezoelectric beam. *Journal of Vibration and Acoustics* 134(1): 011009.
- Staggs J, Ferlemann D and Sheno S (2017) Wind farm security: Attack surface, targets, scenarios and mitigation. *International Journal of Critical Infrastructure Protection* 17: 3–14.
- Tang L, Yang Y and Soh CK (2013) Broadband vibration energy harvesting techniques. In: Elvin N and Erturk A (eds.) *Advances in Energy Harvesting Methods*. New York, NY: Springer New York, pp.17–61.
- Tang L, Zhao L, Yang Y, et al. (2014) Equivalent circuit representation and analysis of galloping-based wind energy harvesting. *IEEE/ASME Transactions on Mechatronics* 20(2): 834–844.
- Tang L and Yang Y (2012) A multiple-degree-of-freedom piezoelectric energy harvesting model. *Journal of Intelligent Material Systems and Structures* 23(14): 1631–1647.
- Wang J, Geng L, Ding L, et al. (2020a) The state-of-the-art review on energy harvesting from flow-induced vibrations. *Applied Energy* 267: 114902.
- Wang J, Tang L, Zhao L, et al. (2020b) Equivalent circuit representation of a vortex-induced vibration-based energy harvester using a semi-empirical lumped parameter approach. *International Journal of Energy Research* 44(6): 4516–4528.
- Wang J, Hu G, Su Z, et al. (2019a) A cross-coupled dual-beam for multi-directional energy harvesting from vortex

- induced vibrations. *Smart Materials and Structures* 28(12): 12LT02.
- Wang J, Tang L, Zhao L, et al. (2019b) Efficiency investigation on energy harvesting from airflows in HVAC system based on galloping of isosceles triangle sectioned bluff bodies. *Energy* 172: 1066–1078.
- Wang J, Zhou S, Zhang Z, et al. (2019c) High-performance piezoelectric wind energy harvester with Y-shaped attachments. *Energy Conversion and Management* 181: 645–652.
- Yan Z, Wang L, Hajj MR, et al. (2020) Energy harvesting from iced-conductor inspired wake galloping. *Extreme Mechanics Letters* 35: 100633.
- Yang K, Wang J and Yurchenko D (2019) A double-beam piezo-magneto-elastic wind energy harvester for improving the galloping-based energy harvesting. *Applied Physics Letters* 115(19): 193901.
- Yang Y and Tang L (2009) Equivalent circuit modeling of piezoelectric energy harvesters. *Journal of Intelligent Material Systems and Structures* 20(18): 2223–2235.
- Yang Y, Zhao L and Tang L (2013) Comparative study of tip cross-sections for efficient galloping energy harvesting. *Applied Physics Letters* 102(6): 064105.
- Yu B (2016) *Nonlinear Dynamics of Cable Galloping Via a Two-Degree-of-Freedom Nonlinear Oscillator*. PhD dissertation. Southern Illinois University at Carbondale Carbondale, Illinois, USA.
- Zhang M, Hu G and Wang J (2020) Bluff body with built-in piezoelectric cantilever for flow-induced energy harvesting. *International Journal of Energy Research* 44(5): 3762–3777.
- Zhao L and Yang Y (2018) An impact-based broadband aeroelastic energy harvester for concurrent wind and base vibration energy harvesting. *Applied Energy* 212: 233–243.